Accurate electron correlation energy functional: Expansion in the interaction renormalized by the random-phase approximation

Mario Benites, Angel Rosado, and Efstratios Manousakis
Department of Physics, Florida State University, Tallahassee, Florida 32306, USA

(Received 21 July 2024; revised 9 October 2024; accepted 12 November 2024; published 26 November 2024)

We present an accurate local density functional for electronic-structure calculations within the density functional theory (DFT). The functional is derived by analyzing the structure of the standard perturbative expansion of the correlation energy of the interacting uniform electron gas. Then, the expansion is partially resummed and reorganized as a self-consistent series in powers of a renormalized electron-electron interaction vertex based on the screened frequency-momentum-dependent dielectric matrix given by the well-known random-phase approximation. First, we demonstrate that the range of r_s, where this reorganized and renormalized series converges, contains and is significantly larger than the average range realized in real crystalline materials. Using a combination of analytical, numerical, and stochastic integration techniques we are able to calculate all the diagrams which have contribution up to the same leading order. We benchmarked the functional using the QUANTUM ESPRESSO implementation of the DFT applied to the same list of materials, selected previously by other authors, in its entirety without any modification of the list. We find that for ground-state properties in general, such as equilibrium atomic distances and bulk moduli, the functional presented here is more accurate than the currently available most popular one.

DOI: 10.1103/PhysRevB.110.195151

I. INTRODUCTION

The density functional theory (DFT) as introduced by Hohenberg, Kohn, and Sham [1,2] (HKS) is broadly used to provide insight into the electronic structure of materials. In addition to the assumed known interaction potential formed by the contribution to the total one-body pseudopotential by all the screened-ionic cores, DFT requires an accurate "exchange-correlation" potential $V_{\rm xc}$. The $V_{\rm xc}$ is a functional of the spatially varying local electronic density field $n(\vec{r})$ produced by the collective presence of all of the electrons in the interacting ground state. In fact, provided that the ground state is not degenerate, one can show the existence of a one-to-one correspondence between the interacting ground state and the diagonal part of the interacting one-body density matrix.

The important feature of this functional is its universal nature, namely, it is the same for all materials. Therefore, one can conceptualize the question of the electronic structure of any given material, as a problem where the response of a system of interacting electrons, in the presence of an external one-body potential presented by the ions, is sought. Its universal character allows us to determine its form, in principle, and at least its local part, by calculating it for the pure system of interacting electrons in the presence of a uniform background of positive charge of density equal to the spatial average of the electronic density (the so-called jellium model).

While this approach of determining the universal density functional by focusing our effort on the Jellium model started more than half a century ago, the ground-state properties of many materials still cannot be calculated with the desired accuracy.

Most functionals, especially the one used by most authors [3–5], are based on an *ad hoc* functional form which is general enough to reduce itself and reproduce the leading terms of extreme $r_s \to 0$ limit of the random-phase approximation (RPA) (a limit which is expected to be captured correctly by the RPA), while the low-density limit (large r_s) and the intermediate regime is fitted to the quantum Monte Carlo results [6] of the jellium model.

However, quantum Monte Carlo (QMC) simulation of fermions is hindered by the infamous sign problem which forces us to limit our calculations to small-size systems of the order of a few hundred [6] or at most several hundred up to one thousand [7,8] electrons. These system sizes are too small to allow extrapolation to the infinite-size limit to remove the finite-size effects to a satisfactory level of accuracy. To give an example of the severity of the finite-size effects, for 368 electrons the occupied states of the noninteracting unpolarized determinant used as part of the initial and guiding trial state in diffusion Monte Carlo, do not have the form of a sphere at all and the kinetic energy of an occupied state on the $k_z = 0$ plane and that of the nearest unoccupied state differ by a $\frac{4}{9}$ fraction of the Fermi energy. Therefore, the simulated system is far away from the actual uniform jellium metallic system and flipping a spin in this simulated-system case costs such a large amount of energy. What is worse is that there is no known scaling function to use in order to extrapolate in the infinite-size limit.

In this work, we illustrate that we should expect a reorganized perturbative expansion, based on using a renormalized RPA-screened interaction vertex, to have a wider range of validity in the parameter r_s than previously thought [9,10]. In fact, we show that the range of r_s, where one should

expect such a reorganized perturbative scheme to be convergent, contains the range of r_s realized in most materials. It is worth noting that, as is well known, using an effective Hamiltonian approach which separates the degrees of freedom into collective (charge-density fluctuations) and elementary excitations above the ground state (quasiparticle/quasihole) one could achieve a very different picture of the rate of convergence [11,12].

We, therefore, undertake a systematically organized perturbation expansion in orders classified by the number of renormalized RPA-screened interaction lines. The correlation energy for any value of the spin polarization and any value of r_s begins with two leading families of diagrams in the RPA-renormalized interaction. The first is the well-known series of rings-of-bubbles-like diagrams and a series which we call the "kite-diagram" series. To determine our functional, first, we very accurately calculate the sum of the ring diagrams for a very wide range of r_s and as a function of spin polarization. We also determine analytically the small r_s and the large r_s singular behaviors of the sum of rings-of-bubbles diagrams. The kite diagram using the bare-Coulomb interaction was first estimated by Gellmann and Brueckner [10] by means of Monte Carlo integration and was later calculated exactly by Onsager [13]. We calculate the correction to the kite-diagram family when a fully RPA-renormalized interaction is used by first carrying out imaginary frequency integrals analytically by appropriately choosing the integration contour in the complex-frequency plane to avoid the branch cut of the dielectric frequency-momentum-dependent function. This allows the remaining 11-dimensional integral to be well behaved for a stochastic integration method to be effective. We find that, in the range of r_s accessible in most materials, this correction previously ignored is as significant as the other contributions to the correlation energy of the interacting electron fluid. The reason for this is that this series of diagrams consists of a contribution to the exchange-correlation energy where the effects of exchange and correlation are both profound and cannot be disentangled.

We then use the numerical results of this calculation and our analytical knowledge of the behavior of the various different terms in the small and large r_s limits to determine a functional form that fits very accurately our numerical results as a function of r_s and spin polarization.

In order to assess the accuracy of our functional relative to the currently popular local density Perdew-Wang (PW) functional [5], we modified the QUANTUM ESPRESSO package [14] to include our functional and we carried out DFT calculations within the local density approximation (LDA) for the same entire list of crystalline materials given in Refs. [15–17] (where the performance of various other functionals was evaluated). We find that our functional overall outperforms the PW functional [5] in the calculation of the equilibrium lattice constants and bulk moduli. These observables are the main indicators of the accuracy of a functional for ground-state properties. We have avoided comparing gaps, as the Kohn-Sham orbitals are only *auxiliary entities* needed in the HKS theory, which is purely a ground-state theory and is not meant to describe *real* single-particle excitations.

The paper is organized as follows. In Sec. II the calculation of the electron gas is described. In Sec. III our functional is presented, while in Sec. IV it is compared with other functionals. In Sec. V its performance is benchmarked. Last, in Sec. VI we give our discussion and our concluding remarks.

II. CALCULATION OF THE CORRELATION ENERGY

In this section we describe how we obtain the ground-state (GS) correlation energy of the homogeneous electron gas for any value of r_s and spin polarization ζ. We will assume a density $n_\uparrow$ of electrons with spin up and $n_\downarrow$ of electrons with spin down with total density $n = n_\uparrow + n_\downarrow$ and

$$\zeta = \frac{n_\uparrow - n_\downarrow}{n_\uparrow + n_\downarrow}, \tag{1}$$

$$r_s = \left(\frac{3}{4\pi n}\right)^{\frac{1}{3}}, \tag{2}$$

with corresponding Fermi wave vector

$$k_{F\sigma} = k_F x_\sigma, \quad k_F \equiv (3\pi^2 n)^{\frac{1}{3}}, \tag{3}$$

where

$$x_\sigma \equiv (1+\sigma\zeta)^{\frac{1}{3}}, \tag{4}$$

and $\sigma = +1, -1$ for spin up and spin down, respectively.

In order to calculate the contributions to the ground-state correlation energy we use the following general expression for the ground-state expectation value of the bare Coulomb interaction term, i.e., $\langle\Psi_0|\hat{V}|\Psi_0\rangle$, where $|\Psi_0\rangle$ is the interacting ground state, for the electron gas of spin polarization ζ:

$$\langle\Psi_0|\hat{V}|\Psi_0\rangle = -\frac{i\hbar V}{2}\int_0^1 \frac{d\lambda}{\lambda}\int \frac{d^4k}{(2\pi)^4} e^{ik^0\eta}\mathrm{Tr}[\Sigma^{*\lambda}G^\lambda], \tag{5}$$

where $\Sigma^{*\lambda} = \Sigma^{*\lambda}_{\alpha\beta}(\vec{k}, k^0)$ and $G^\lambda = G^\lambda_{\alpha\beta}(\vec{k}, k^0)$ are the proper self-energy and the fully interacting fermion propagator tensors, respectively, under the rescaling of the coupling of the interaction: $e^2 \to \lambda e^2$, where λ guarantees the interaction to be turned on very slowly in the system. The α and β are spin indices (with values of 1 or -1) and η is an infinitesimal factor with time dimension that preserves the correct time order of the field operators when evaluating expectation values. Both tensors are diagonal in this system since the electron's spin is conserved at the vertex level in the Coulomb interaction.

A. Issues and history of the perturbative expansion

Figure 1 gives the ground-state energy correct up to leading order in the bare Coulomb interaction. Figure 1(a) is the Hartree-Fock approximation where the first term is the Hartree term, which, in the case of our jellium model, is canceled by the uniform background of positive charge. Figure 1(b) gives the next-order correction, which is the correlation energy in leading order in the bare Coulomb interaction. The first diagram of Fig. 1(b) alone is infinite at any value of r_s because of the singular nature of the Coulomb interaction in the infrared. The second diagram of Fig. 1(b) is zero and the third has been first estimated by Gellmann and Brueckner [10] by means of Monte Carlo integration and was later calculated exactly by Onsager [13]. In the rest of this paper, we will refer to this latter diagram as the "kite" diagram.

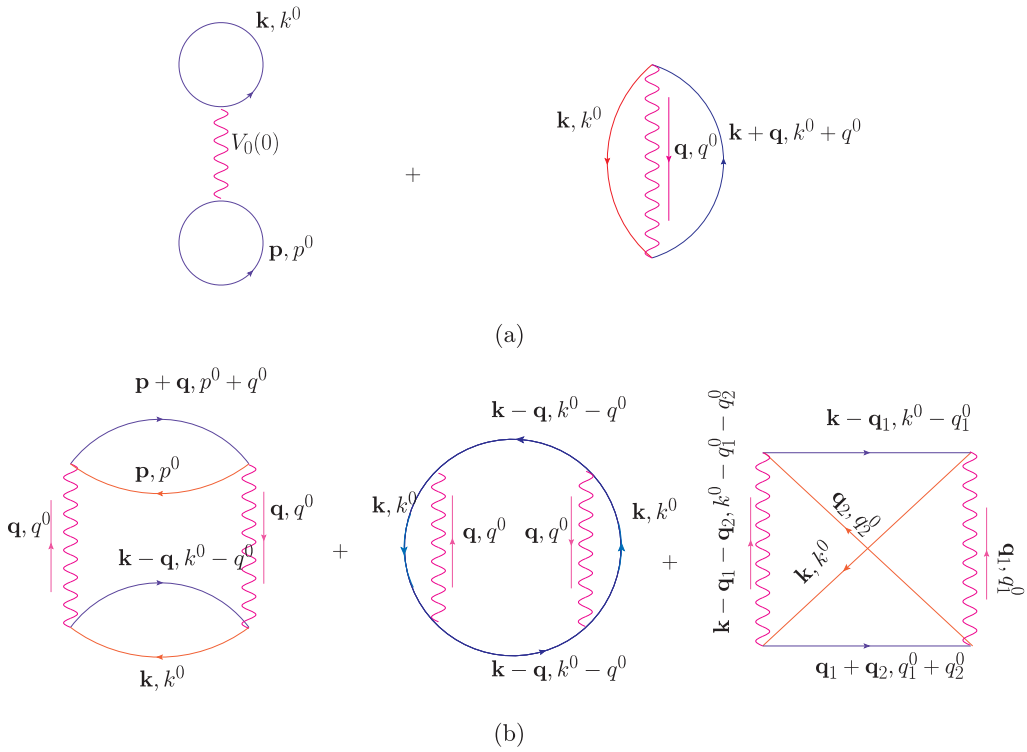

FIG. 1. (a) First order in the bare Coulomb interaction. (b) Second order, i.e., the correlation energy correct up to leading order in bare Coulomb interaction.

In order to "bypass" the problem of the infinite character of the first diagram of Fig. 1(b), what has been done was to replace one of the interacting lines by the renormalized interaction line given by the RPA sum of ring diagrams [10,18,19] shown in Fig. 2 and this makes this renormalized diagram finite at any finite value of r_s and it diverges as $\ln(r_s)$ in the $r_s \to 0$ limit.

The above series of all the correlation diagrams is the RPA, which leads to dressing one of the interaction lines as shown in Fig. 2. This effective interaction line introduces an emerging regulator which endows the new diagram with a finite value at finite r_s.

Hence, a perturbation expansion in the bare Coulomb interaction leads to infinities and it is necessary to renormalize the Coulomb interaction. Therefore, the entire perturbation expansion needs to be systematically reorganized in terms of such a renormalized interaction.

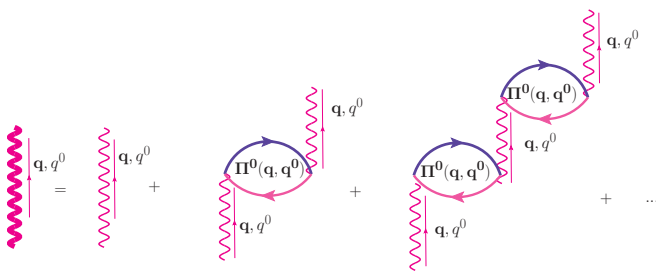

FIG. 2. The bold interaction line represents the sum of the terms included in the RPA and each loop $[\Pi^0(q, q^0)]$ represents the spin trace of the polarization tensor. For more details see text.

B. Summation of the ring diagrams

First, we summarize the calculation for the well-known RPA approach [10,18,19]. The fundamental aspect of this theory is that it renormalizes the bare Coulomb interaction by adding together the selected terms of the perturbation expansion illustrated in Fig. 2 which defines an effective interaction with a Fourier transform given as follows:

$$\tilde{V}_{\text{eff}}(q, q^0) \equiv \frac{4\pi e^2}{q^2 \epsilon(q, q^0)}, \tag{6}$$

where the dielectric function $\epsilon(q, q^0)$ is found by calculating the spin trace of the polarization $\Pi^0_{\sigma\sigma'}(q, q^0)$ (bubble or particle-hole diagram):

$$\epsilon(q, q^0) = 1 - \frac{4\pi e^2}{q^2} \sum_{\{\sigma\}=\pm} \Pi^0_\sigma(q, q^0), \tag{7}$$

where one spin index σ is dropped in the polarization tensor since it is diagonal, and $\Pi^0_\sigma(q, q^0)$ can be calculated by a four-dimensional integral of a product of two Green's functions, which the result yields an even function in frequency q^0. The integral expression of $\Pi^0_\sigma(q, q^0)$ is given by

$$\Pi^0_\sigma(q, q^0) = \frac{-i}{\hbar} \int \frac{d^4k}{(2\pi)^4} G^0_\sigma(k^\mu + q^\mu) G^0_\sigma(k^\mu), \tag{8}$$

where the μ superscript is used only as a shorthand notation for $q^\mu = (\vec{q}, q^0)$ (not to be confused as a covariant quantity) and the noninteracting Green's function has the usual integral expression that takes into consideration the energy dispersion $\epsilon_{\vec{k},\sigma}$ of the electron measured relative to the chemical potential

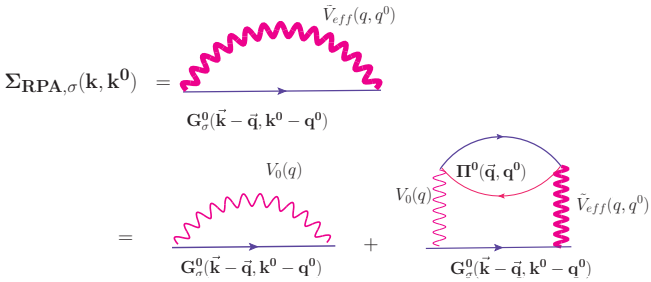

FIG. 3. The self-energy within the RPA. We have not included the Hartree term as it is canceled by the contribution of the uniform positive background in the jellium model.

with spin σ. At zero temperature we have

$$G^0_\sigma(k^\mu) = \frac{\Theta(k-k_{F\sigma})}{k^0 - \frac{\epsilon_{\vec{k},\sigma}}{\hbar} + i\eta} + \frac{\Theta(k_{F\sigma}-k)}{k^0 - \frac{\epsilon_{\vec{k},\sigma}}{\hbar} - i\eta}. \tag{9}$$

The calculation of the polarization tensor is similar to the spin-unpolarized case, where the latter is solved in Refs. [20–22]. The difference in the calculation is at the level of rescaling the wave vector $\vec{q}$ and frequency q^0 into unitless variables, but instead of using k_F for the rescaling, we use $k_{F\sigma}$. The result for $\Pi^0_\sigma(q,q^0)$ depends on the Lindhard's function where its real and imaginary parts can be found in Refs. [20,21]. In the following discussion, we will involve the expression of its analytic continuation in imaginary frequency [see our Eq. (14)].

The self-energy $\Sigma_{\mathrm{RPA},\sigma}(k,k^0)$ within the RPA is illustrated in Fig. 3 and when multiplied by the noninteracting Green's function, i.e., $G^0_\sigma(k,k^0)$, as in expression given by Eq. (5), and integrated over the external leg variables frequency (k^0), and wave vector ($\mathbf{k}$) it gives the ground-state expectation value of the interaction energy. The first term is the exchange (Fock) diagram and only the second term contributes to the correlation energy. Once this step is done, this yields the sum of the ring diagrams with partial spin polarization (ζ), which consists of summing all of the first-order Goldstone diagrams within the RPA, as listed in Fig. 4. The calculation of these ring diagrams consists of carrying out a calculation of a five-dimensional integral, one integration over the λ parameter, and the other four-dimensional integrals along the frequency variable q^0 and the wave vector $\vec{q}$. After performing a simple integral along the λ parameter on the integral expression of the ring-diagram series, and by rescaling the wave vector and

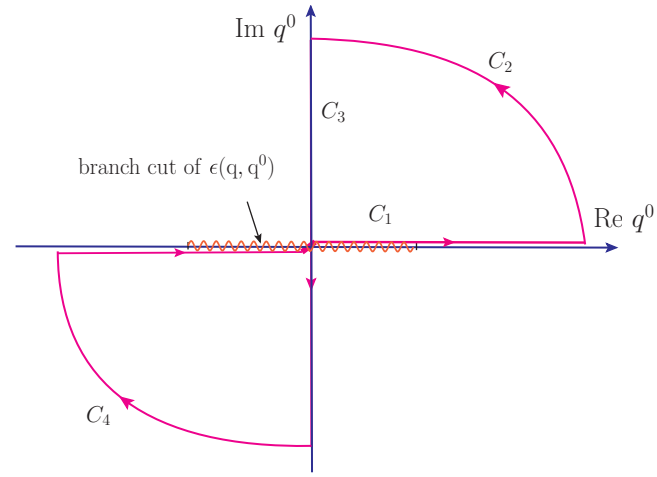

FIG. 5. The path on the complex frequency plane chosen for the calculation of the contribution to the ring-diagram series (see text).

frequency variables by the mapping $\vec{q} \to k_f\vec{\kappa}$, $q^0 \to \hbar k_F^2 \nu/m$, one obtains the general expression for the contribution to the ring-diagram series $E_r(r_s,\zeta)$ as follows:

$$E_r(r_s,\zeta) = \frac{Ne^2}{2a_0}\epsilon_r(r_s,\zeta), \tag{10}$$

where the contribution to the ground-state energy per particle in Ry, i.e., $\epsilon_r(r_s,\zeta)$, is given by the following four-dimensional integral:

$$\epsilon_r(r_s,\zeta) = \frac{-3i}{16\alpha^2\pi^2 r_s^2}\int d^3\kappa \int_{-\infty}^{\infty} d\nu[\ln(\epsilon_d)+1-\epsilon_d], \tag{11}$$

where $\alpha = [4/(9\pi)]^{1/3}$ and $\epsilon_d = \epsilon(k_F\kappa, \frac{\hbar k_F^2}{m}\nu)$. We can proceed to choose a particular complex contour to map the rescaled frequency integral along the real line into a pure imaginary frequency integration $i\nu$ in a way that does not enclose the branch cuts that arise from the logarithmic terms that come from the dielectric function, as seen in Fig. 5. In this case, we use the analytic continuation of the Lindhard function where the expression is more simplified since this yields a real function. After some simplification of the expression of the integrand for the ring-diagram series per particle by using

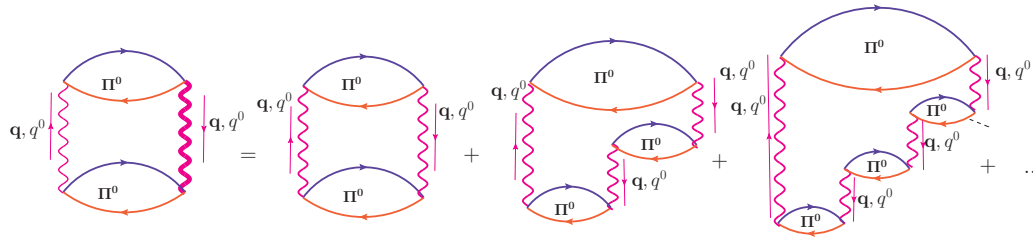

FIG. 4. The sum of the series of diagrams depicted in the right-hand side of the equation in the figure is the correlation energy within RPA and it corresponds to replacing one of the interaction lines in the first diagram of Fig. 1 with a bold interaction line which is symbolically depicted by the diagram in the left-hand side of the equation. In this figure we labeled Π^0 as the spin trace of the polarization tensor.

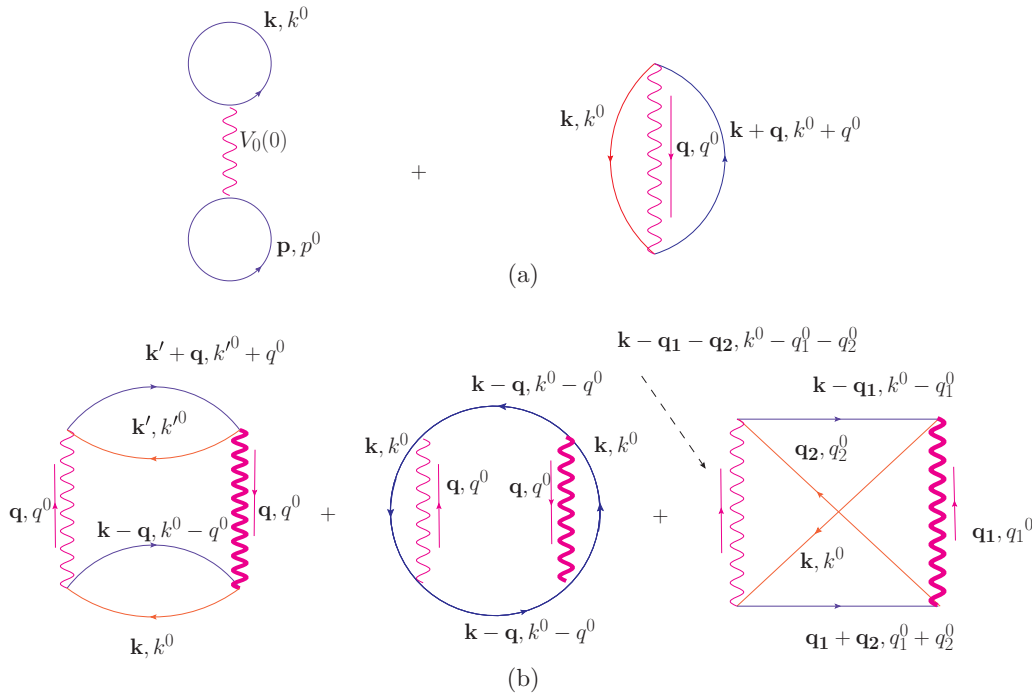

FIG. 6. (a) The zeroth-order diagrams to the total ground-state energy in the RPA-renormalized interaction. (b) The set of all the diagrams contributing to the first order in the RPA-renormalized interaction.

$x = \nu/\kappa$, we are left with an imaginary frequency integration given by

$$\epsilon_r(r_s,\zeta) = \gamma \int_0^\infty d\kappa\, \kappa^3 \int_0^\infty dx[\ln(1+\tilde{\Pi}) - \tilde{\Pi})], \tag{12}$$

$$\tilde{\Pi} \equiv \frac{\alpha r_s}{\pi \kappa^2} \sum_\sigma x_\sigma(\zeta) g\left(\frac{\kappa}{x_\sigma(\zeta)}, i\frac{\kappa x}{x_\sigma^2(\zeta)}\right), \tag{13}$$

where $\gamma = \frac{3}{2\pi\alpha^2 r_s^2}$, and the analytic continuation of the Lindhard function is given by the following expression:

$$g(q_1, i\nu) = 1 + \frac{\nu^2 + \kappa_+\kappa_-}{2q_1^3} \ln\left(\frac{\kappa_+^2+\nu^2}{\kappa_-^2+\nu^2}\right) - \frac{\nu}{q_1}\left[\tan^{-1}\left(\frac{\kappa_+}{\nu}\right) + \tan^{-1}\left(\frac{\kappa_-}{\nu}\right)\right], \tag{14}$$

where $\kappa_\pm = q_1 \pm q_1^2/2$. We used the integral expression given by Eq. (12) to calculate numerically the ring-diagram series per particle $\epsilon_r(r_s,\zeta)$ by using integration by quadrature. As in the ring-diagram series of the unpolarized case, $\epsilon_r(r_s,\zeta)$ also has a $\ln(r_s)$ divergent part which we were able to calculate analytically by keeping track of the integral on regions of integration of very small q. Such calculation gives rise to the generalized coefficient of this divergent part, given by

$$\epsilon_r(r_s,\zeta) = c_L(\zeta)\ln(r_s) + c_0(\zeta), \tag{15}$$

where $c_L(\zeta)$ is the coefficient of the $\ln(r_s)$ term given by

$$c_L(\zeta) = \frac{1}{\pi^2}\left[(1-\ln 2) + \frac{x_+x_-}{2}\chi - \ln(\chi) + \frac{1}{2}\sum_\sigma x_\sigma^3 \ln(x_\sigma)\right], \tag{16}$$

where

$$\chi(\zeta) = \sum_\sigma x_\sigma(\zeta), \tag{17}$$

and $x_\sigma(\zeta)$ is given by Eq. (4). We will use this expression in our functional.

C. RPA-renormalized perturbation expansion

We wish to carry out a perturbation expansion in the RPA-renormalized Coulomb interaction as in Hedin [23]. We are not regarding this expansion as an r_s expansion. We regard it as an expansion in powers of the renormalized interaction.

As stated earlier, our goal is to compute by a perturbative expansion the total ground-state expectation value of the interaction energy, i.e., the expectation value of the bare Coulomb interaction (as it appears in the original many-body Hamiltonian) in the interacting ground-state wave function, i.e.,

$$\langle\Psi_0|\hat{V}|\Psi_0\rangle = \langle\Psi_0|\sum_{i<j}\frac{e^2}{r_{ij}}|\Psi_0\rangle, \tag{18}$$

where $|\Psi_0\rangle$ is the interacting ground state. This was our starting computational goal [as set originally by Eq. (5)]. This series up to the first order in the RPA-renormalized interaction line is shown in Fig. 6. Figure 6(a) lists all the zeroth-order terms contributing to the ground-state interaction energy. The presence of the bare Coulomb interaction line should not be confused with the first order, it is the operator of which we compute the expectation value of, it is not coming from the expansion of the interacting ground state. The diagrams contributing to the ground-state interaction energy (and correlation energy) to leading order in the RPA-renormalized interaction are shown in Fig. 6(b). Notice

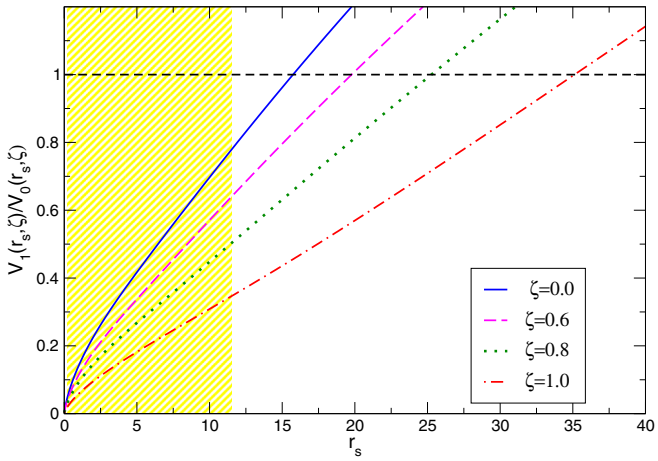

FIG. 7. Comparison of the first-order contribution to the zeroth-order contribution to the interaction energy in RPA-renormalized interaction line.

that one bare Coulomb interaction line is unavoidable and cannot be dressed by the RPA effective interaction. The reason is that the interaction energy is calculated as the expectation value in the interacting ground state of the bare Coulomb interaction. Namely, this bare interaction line is the observable to which the ground-state expectation value is computed within perturbation theory. The other lines can be renormalized because they come from the Goldstone expansion of the ground state. Now, we note that the second diagram in Fig. 6(b) is identically equal to zero. The reason is because there is the product of two bare fermion propagators, a particle of four-momentum $(\mathbf{k}, k^0)$, and a hole propagator with the same four-momentum.

The two zeroth-order diagrams are the familiar Hartree (which cancels the interaction of the electron gas with the uniform positive background) and the bare exchange terms contributing to the total density functional. The exchange term is a well-known contribution to the interaction energy per particle, which in Ry is given by

$$V_0(r_s,\zeta) = -3\frac{\sum_\sigma x_\sigma^4}{4\pi\alpha r_s}, \tag{19}$$

with x_σ defined by Eq. (4).

The first diagram of Fig. 6(b) is the sum of all the ring-diagram series which was computed in the the previous section. The third diagram, which we call "the kite diagram" because of its shape, is calculated in the following section.

Our series expansion of the interaction energy, i.e., the quantity which we calculate can be written as

$$\langle\Psi_0|\hat{V}|\Psi_o\rangle = V_0(r_s,\zeta) + V_1(r_s,\zeta) + V_2(r_s,\zeta) + \cdots, \tag{20}$$

where $V_n(r_s,\zeta)$ denotes the nth order in the RPA-renormalized interaction. Namely, $V_n(r_s,\zeta)$ contains only n of such lines. Such a series will converge fast as long as $|V_{n+1}(r_s,\zeta)| \ll |V_n(r_s,\zeta)|$. Using the final results of our calculation we can provide a justification of the validity of this expansion using the known results for $n=0$ and our results for $n=1$. Figure 7 provides the ratio $V_1(r_s,\zeta)/V_0(r_s,\zeta)$ for various values of the spin-polarization parameter ζ. Given that this ratio is significantly smaller than unity in the region of r_s realized in most real materials, we should expect to have a converging series of our expansion in such region and our functional to be a good approximation for direct application to real materials. We note that we checked in the charge density output file of the QE calculation and we did not find any value of density listed in the file which corresponds to a value of r_s, which lies outside the yellow-shaded region of this figure.

Therefore, we conclude that using the screened (and, therefore weaker) RPA-renormalized interaction vertex should lead to a converging perturbative expansion in the region of r_s and ζ realized in most real materials.

D. Summation of the kite-diagram series

This section will briefly explain how to obtain an integral expression for the kitelike-diagram series that contributes to the ground-state (GS) energy of the homogeneous spin-polarized electron gas, where more details concerning the calculation are given in Appendix C. This term is first order in terms of the cluster expansion, where the integral expression of such a term is found by calculating the expectation value of the bare Coulomb potential operator $\langle\Psi_0|\hat{V}|\Psi_0\rangle$ [our calculation begins from Eq. (5)]. Therefore, the bare interaction line represents the operator and the other line is due to the expansion. Our expansion resums a selected series of diagrams illustrated in Fig. 2 resulting in the renormalization of the second interaction line to become an RPA-dressed interaction line.

The calculation of the kite diagram involves computing the diagram series illustrated in Fig. 8. As seen in this figure, we separate the zeroth order of the expansion of the renormalized interaction line (first diagram) from the correction to the kite diagram which carries a r_s dependence given by the dielectric function included in the Goldstone diagram (second diagram). We used Eq. (5) to calculate both contributions to the Goldstone diagram within renormalization, as explained in Appendix C. The expression for the complete kite diagram within renormalization is then written as

$$E_{2b}[n_\uparrow, n_\downarrow] = E^0_{2b}[n_\uparrow, n_\downarrow] + \Delta E_{2b}[n_\uparrow, n_\downarrow], \tag{21}$$

where the first term corresponds to the kite diagram having two bare interaction lines which come from the leading term of the effective Coulomb interaction that comes from the renormalization in RPA, while the second term corresponds to the kite-diagram correction given by the single renormalized interaction line. Their corresponding expressions are given below:

$$E^0_{2b}[n_\uparrow, n_\downarrow] = \frac{iV}{2\hbar}\int_0^1 d\lambda\,\lambda \int \frac{d^4k}{(2\pi)^4}\int\frac{d^4q_1}{(2\pi)^4} \times \int \frac{d^4q_2}{(2\pi)^4} e^{ik^0\eta} V_0(\vec{k}-\vec{q}_1-\vec{q}_2)V_0(\vec{q}_1)\tilde{D}, \tag{22}$$

$$\Delta E_{2b}[n_\uparrow, n_\downarrow] = \frac{iV}{2\hbar}\int_0^1 d\lambda\,\lambda^2 \int \frac{d^4k}{(2\pi)^4}\int\frac{d^4q_1}{(2\pi)^4} \times \int \frac{d^4q_2}{(2\pi)^4} \frac{e^{ik^0\eta} V_0(\vec{k}-\vec{q}_1-\vec{q}_2)V_0^2(\vec{q}_1)\Pi^0(q_1,q_1^0)\tilde{D}}{\epsilon_\lambda(q_1,q_1^0)}, \tag{23}$$

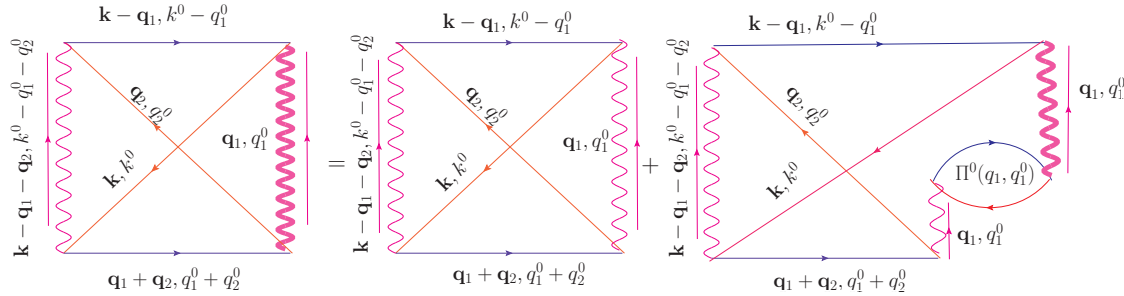

FIG. 8. The kite-diagram series can be broken into two parts. The first consists of using the bare Coulomb interaction. This diagram was first estimated by Gellmann-Brueckner by means of Monte Carlo integration and it was later calculated exactly by Onsager [13]. The second, which is r_s and ζ dependent, is calculated in this paper.

where

$$\tilde{D} \equiv \sum_{\sigma=\pm} G_\sigma^0(\vec{q}_1+\vec{q}_2, q_1^0+q_2^0) G_\sigma^0(\vec{q}_2, q_2^0) \times G_\sigma^0(\vec{k}-\vec{q}_1, k^0-q_1^0) G_\sigma^0(\vec{k}, k^0), \tag{24}$$

and $\epsilon_\lambda(q_1, q_1^0)$ is the dielectric function given by Eq. (7) with the interaction coupling rescaled by $e^2 \to \lambda e^2$.

By means of a dimensional analysis of the contribution to the ground-state energy given by Eq. (22), it can be shown that it is independent of r_s, which implies that it is independent of the relative spin polarization ζ. Its contribution is just a constant independent of r_s and it has the same value as in the unpolarized case, which Onsager previously obtained and it is given by [13]

$$E_{2b}^0[n_\uparrow, n_\downarrow] = \frac{Ne^2}{2a_0}\epsilon_{2b}^0, \tag{25}$$

where the energy per particle is given in Ry as

$$\epsilon_{2b}^0 = \frac{\ln(2)}{3} - \frac{3}{2\pi^2}\zeta(3) \approx 0.048\,36. \tag{26}$$

The correction to the kite diagram is the piece that contains the ζ and r_s dependence and this Goldstone diagram cannot be computed accurately by using the Monte Carlo integration technique directly by using the expression given by Eq. (23) due to the so-called "sign" problem that comes at the level of the frequency integrals of the product of the Green's function. It is possible to get around this problem by isolating the momentum and frequency associated with the renormalized interaction line and doing the integrals of the remainder frequency variables, which the dielectric function is independent of, by using Cauchy's theorem. Also, as explained in Appendix C, to make the integrand more compact, we had to rely on a sequence of transformations of the dummy wave-vector integration variables which helped us reduce the number of integrals to calculate numerically using the Monte Carlo integration technique. The integral also becomes easier to handle when applying similar transformations than we did in the case of the ring-diagram series (check Appendix C for more details). We chose the same complex contour path on the complex plane (see Fig. 9) which avoids enclosing the branch cuts of the dielectric function [24] and the poles that come from the denominator part of the noninteracting Green's function, we can map the frequency integral contained in the argument of the dielectric function along the real line into an integral along the imaginary line. The last step is to do a dimensional analysis, as done for the ring-diagram series which allows us to factor out the total number of electrons in the correction of the kite-diagram series, which allows us to write this ground-state energy contribution in terms of an energy-per-particle factor:

$$\Delta E_{2b}[n_\uparrow, n_\downarrow] = \frac{Ne^2}{2a_0}\Delta\epsilon_{2b}[n_\uparrow, n_\downarrow], \tag{27}$$

where the energy per particle of the correction of the kite diagram within renormalization is given by the sum of two major contributions which are given as

$$\Delta\epsilon_{2b,1} = \int_0^1 d\lambda \int d^3q_1 \int_{k\leqslant 1} d^3k \int_{q_2\leqslant 1} d^3q_2 \sum_\sigma \int_0^{\frac{\pi}{2}} du\, \mathcal{L}\frac{f_\lambda^\sigma(\vec{q}_1, a(\vec{q}_1,\vec{q}_2)\tan(u),\zeta) - f_\lambda^\sigma(\vec{q}_1, a(\vec{q}_1,\vec{k})\tan(u),\zeta)}{|\vec{k}-\vec{q}_2|^2(a(\vec{q}_1,\vec{q}_2)-a(\vec{q}_1,\vec{k}))}, \tag{28}$$

$$\Delta\epsilon_{2b,2} = -\int_0^1 d\lambda \int d^3q_1 \int_{k\leqslant 1} d^3k \int_{q_2\leqslant 1} d^3q_2 \sum_\sigma \int_0^{\frac{\pi}{2}} du\, \mathcal{L}\frac{f_\lambda^\sigma(\vec{q}_1, a(\vec{q}_1,\vec{q}_2)\tan(u),\zeta) + f_\lambda^\sigma(\vec{q}_1, a(\vec{q}_1,\vec{k})\tan(u),\zeta)}{|\vec{k}+\vec{q}_1+\vec{q}_2|^2(a(\vec{q}_1,\vec{q}_2)+a(\vec{q}_1,\vec{k}))}, \tag{29}$$

where

$$\mathcal{L} \equiv \frac{3\alpha r_s}{16\pi^7}\frac{\lambda^2}{q_1^4}\Theta(|\vec{q}_1+\vec{q}_2|-1)\Theta(|\vec{k}+\vec{q}_1|-1), \tag{30}$$

and the term $a(\vec{q}_1, \vec{q}_2)$ is related with the relative differences between the energy dispersion of the electrons:

$$a(\vec{q}_1, \vec{q}_2) = \frac{|\vec{q}_1+\vec{q}_2|^2 - q_2^2}{2}. \tag{31}$$

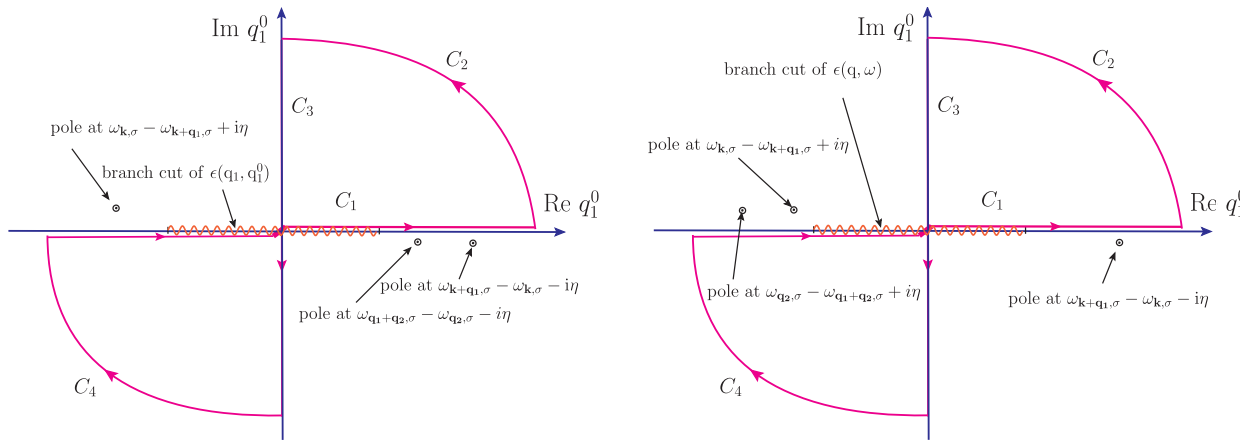

FIG. 9. The paths we chose to calculate the two contributions Δ_1 and Δ_2 to the kite-diagram series. Both avoid enclosing the branch cut of the dielectric function and the single poles of the noninteracting Green's functions.

A last integration mapping had to be done to smooth out the frequency integrand to get more precise numerical results for the correction to the kite diagram $\Delta\epsilon_{2b}[n_\uparrow, n_\downarrow]$. Such mapping is what yields an expression for the integrands in terms of the function $f_{\lambda,\sigma}(\vec{q}_1, \nu, \zeta)$, which is defined as

$$f_\lambda^\sigma(\vec{q}_1, \nu, \zeta) \equiv \sum_{\sigma'} \frac{x_\sigma^3 x_{\sigma'} g(\theta q_1, \theta^2 z)}{x_\sigma^2 + \frac{\lambda\alpha r_s}{\pi q_1^2} \sum_{\sigma''} x_{\sigma''} g\left(\theta_2 q_1, \theta_2^2 z\right)}, \tag{32}$$

where $z = i\nu$, $\theta \equiv x_\sigma / x_{\sigma'}$, and $\theta_2 \equiv x_\sigma / x_{\sigma''}$. The expressions given by Eqs. (28) and (29) are the definite expressions that we used to do the Monte Carlo integration. The number of sample points used was $N_b = 10^9$ to reduce the statistical uncertainty given by the stochastic method used. The data that were obtained were later combined along with the numerical data obtained for the ring-diagram series and Onsager's value ϵ_{2b}^0 to obtain the numerical data for the correlation energy $\epsilon_c(r_s, \zeta)$ for several values of ζ and r_s. This was important to obtain an interpolation function for the coefficients of the expansion in r_s of the correlation energy.

E. Checking our calculation

Our calculations of the ring-diagram series agree well with Hedin's reported results within his large error bars. However, our results are of much higher precision as we have more powerful computational resources compared to those available at the time of Hedin's paper [23].

We have verified the results of the full-kite-diagram series using various numerical checks discussed in this subsection. In addition, we used analytical results obtained at certain extreme limits to check that the results of our Monte Carlo calculations are correct.

First, to verify our numerical results from our Monte Carlo code, we asked another member of our research group (named in the Acknowledgments section) to independently calculate the full-kite diagram by using Eqs. (28) and (29) and by writing a different Monte Carlo code. The results agree with ours within the Monte Carlo error.

We have also derived a different expression for the kite-diagram series of $\epsilon_{2b}(r_s, \zeta)$ starting from the full expression without separating the contribution of the Onsager kite (i.e., the $r_s \to 0$ limit) and carrying out the frequency integral by avoiding the branch cuts from the dielectric function to obtain the different expression in the same way as for the correction to the full-kite-diagram series explained in Appendix C. The new expression of the full-kite-diagram series that we found is given by

$$\epsilon_{2b}(rs, \zeta) = \epsilon_{2b}^1(rs, \zeta) + \epsilon_{2b}^2(r_s, \zeta), \tag{33}$$

where the expressions for $\epsilon_{2b}^1(rs, \zeta)$ and $\epsilon_{2b}^2(rs, \zeta)$ are given by

$$\epsilon_{2b,1} = -\int_0^1 d\lambda \int d^3q_1 \int_{k\leqslant 1} d^3k \int_{q_2\leqslant 1} d^3q_2 \sum_\sigma \int_0^{\frac{\pi}{2}} du\, \mathcal{A} \frac{M_\lambda^\sigma(\vec{q}_1, a(\vec{q}_1, \vec{q}_2)\tan(u), \zeta) - M_\lambda^\sigma(\vec{q}_1, a(\vec{q}_1, \vec{k})\tan(u), \zeta)}{|\vec{k} - \vec{q}_2|^2 (a(\vec{q}_1, \vec{q}_2) - a(\vec{q}_1, \vec{k}))}, \tag{34}$$

$$\epsilon_{2b,2} = \int_0^1 d\lambda \int d^3q_1 \int_{k\leqslant 1} d^3k \int_{q_2\leqslant 1} d^3q_2 \sum_\sigma \int_0^{\frac{\pi}{2}} du\, \mathcal{A} \frac{M_\lambda^\sigma(\vec{q}_1, a(\vec{q}_1, \vec{q}_2)\tan(u), \zeta) + M_\lambda^\sigma(\vec{q}_1, a(\vec{q}_1, \vec{k})\tan(u), \zeta)}{|\vec{k} + \vec{q}_1 + \vec{q}_2|^2 a(\vec{q}_1, \vec{q}_2) + a(\vec{q}_1, \vec{k}))}, \tag{35}$$

where $\mathcal{A} = (\mathcal{L}\pi q_1^2)/(\lambda\alpha r_s)$, $\mathcal{L}$ was given in Eq. (30), while the $\mathcal{M}_\lambda^\sigma(\vec{q}_1, \nu, \zeta)$ is expressed as

$$M_\lambda^\sigma(\vec{q}_1, \nu, \zeta) \equiv \frac{x_\sigma^5}{x_\sigma^2 + \frac{\lambda\alpha r_s}{\pi q_1^2} \sum_{\sigma'} x_{\sigma''} g\left(\theta_2 q_1, \theta_2^2 z\right)}, \tag{36}$$

where $z = i\nu$ and $\theta_2 \equiv x_\sigma / x_{\sigma''}$. The numerical results that we have obtained by using Eqs. (34) and (35) agree within the Monte Carlo error for various values of ζ and r_s with the results obtained as explained in the previous section. We have also used these expressions to calculate the kite-diagram

TABLE I. Coefficients of ϵ_{2b} fitted to Eq. (39) in Ry. The coefficient C_2 for ϵ_{2b} is close to the coefficient reported in Ref. [25]. The fit was done for values of r_s from 0 to 1.

	C_1	C_2	C_3
ϵ_{2b}	0.01212	−0.02083	−0.00562

series at $r_s = 0$ and they yield Onsager's value within the 1% error. In addition, we have worked on a code that uses the importance sampling algorithm with the goal of reducing our current numerical error by using the Monte Carlo algorithm, and it yields similar values for $\epsilon_{2b}(r_s, \zeta)$ reported in Table IX within the error bars.

A consistency check of our analytical expressions for $\epsilon_{2b}(r_s, \zeta)$ is obtained by using Onsager's value ϵ^0_{2b} and both expressions from Eqs. (28) and (29), and calculating the limits of $r_s \to 0$ and $r_s \to \infty$. We have also done an internal consistency check using a different expression for the full-kite-diagram series given by Eqs. (33)–(35) for these two limits.

Our analytical result for the correction to the full-kite diagram for every value of partial spin polarization ζ, obtained from the sum of the two terms from Eqs. (28) and (29), also has the correct asymptote at $r_s \to \infty$. In this limit, the function $f^\sigma_\lambda(\vec{q}, \nu, \zeta)$ from Eq. (32) yields the following expression:

$$f^\sigma_\lambda(\vec{q}_1, \nu, \zeta) \overset{r_s\to\infty}{\approx} \frac{\pi q_1^2(1+\sigma\zeta)}{\lambda\alpha r_s}, \tag{37}$$

where the sum over the spin variable σ on this function is independent of ζ. By inserting Eq. (37) in (28) and (29), we find that $\Delta\epsilon_{2b,1}$ yields zero, while $\Delta\epsilon_{2b,2}$ is the surviving term that yields the same expression as Onsager's integral expression of ϵ^0_{2b}, but with the opposite sign. In the limit $r_s \to \infty$, we have

$$\Delta\epsilon_{2b,2} \overset{r_s\to\infty}{\approx} -\epsilon^0_{2b}, \tag{38}$$

where this limit implies that the full-kite diagram yields zero in the limit $r_s \to \infty$ when Onsager's result is added.

It is trivial to check that both corrections to the full-kite-diagram series, at $r_s = 0$, are also zero since both terms from Eqs. (28) and (29) have a r_s global factor. The expression from Eq. (36) is equal to x^3_σ at $r_s = 0$, which is substituted in both expressions (34) and (35). After doing the substitution, only the term $\epsilon_{2b,1}$ is equal to zero, while $\epsilon_{2b,2}$ yields the Onsager's integral expression [13] after doing the integral over the variable u and the sum over the spin σ.

We also extracted the coefficient of $r_s \ln r_s$ in the small r_s limit to the value reported analytically [25] (a value of 0.013 04 Ry) as follows. We fit the full-kite-diagram Monte Carlo data from Table IX to the following small r_s expansion:

$$\epsilon_{2b}(r_s) = \epsilon^0_{2b} + C_1 r_s \ln r_s + C_2 r_s + C_3 r_s^2 \ln(r_s). \tag{39}$$

The results of the fit are given in Table I. Notice that the coefficient C_1 is in reasonable agreement with the exact value [25]. As we will discuss in the following subsection and in Sec. IV B that SOSEX and PW give a much different (by about a factor of 2) value for this coefficient. We feel that this is a strong test that our calculation of the kite-diagram series was done correctly.

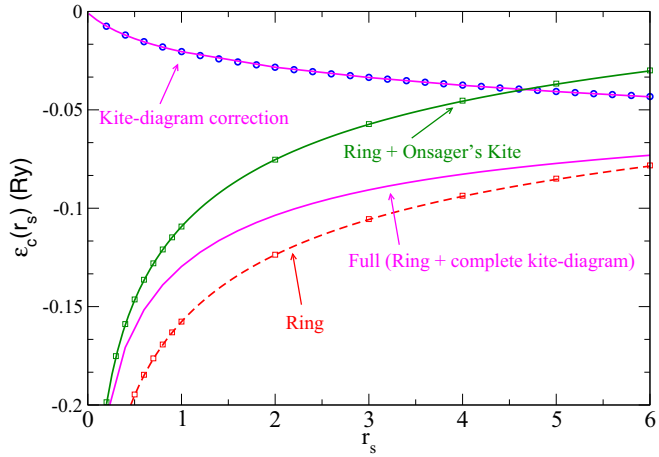

FIG. 10. The contribution of the various terms to the correlation energy as a function of r_s.

F. Comparison of the contributions

Here we wish to compare the various contributions to the correlation energy at the leading order of the RPA renormalized interaction. Namely, the sum of the ring diagrams, the simple contribution of the bare-kite diagram calculated by Onsager, and the full-kite diagram as calculated here numerically.

The various levels of approximation and the relative significance of each term are demonstrated in Fig. 10 as a function of r_s for $r_s < 6$. The correlation energy obtained by including only the ring diagrams is shown by the red dashed line. Adding the r_s-independent contribution of the kite diagram, as calculated by Onsager exactly, to the sum of the ring diagrams gives rise to the solid green line. The full calculation is shown by the purple solid line where we have added the r_s-dependent correction to the kite (open circles).

III. OUR FUNCTIONAL

In this section we present our functional form obtained by fitting the results discussed in the previous sections to analytic forms for a straightforward inclusion in the present implementations of the DFT. Because our results are based on a order-by-order expansion in the number of RPA-renormalized interaction lines, we name this functional and will refer to it in the future as RPA-based functional (RPAF).

The correlation energy per particle $\epsilon_c(r_s, \zeta)$ calculated within the RPA is given by the sum of the two Goldstone diagrams within the first order of the reorganized perturbative expansion: $\epsilon_{2b}(r_s, \zeta)$ and $\epsilon_r(r_s, \zeta)$.

The data for the ring-diagram series per particle $\epsilon_r(r_s, \zeta)$ have been obtained by integration by adaptive quadrature, which yields a more precise calculation in contrast to the numerical results of the integrals of the correction of the kite-diagram series within the RPA, which was obtained with Monte Carlo integration technique and it is explained in Appendix C.

It is very important to have an analytic expression for the coefficient of the $\ln(r_s)$ for any value of ζ because it diverges for $r_s \to 0$ and it continues to be a large part of the functional for values of r_s in the physically realizable region. This is done

TABLE II. First (second) column: The values of the coefficient c_0 (e_1) obtained by fitting the small (large) r_s part of our data to the form (40) [Eq. (41)] for various values of ζ. Third and fourth columns give the values of the coefficients a_2 and b_2 entering the functional form for $\epsilon_r(r_s, \zeta)$ [Eq. (42)] obtained by fitting our data to this form under the constraints [Eqs. (47)–(50). See text for details.

ζ	c_0 (Ry)	e_1 (Ry)	a_2	b_2
0.00	−0.1423	0.8822	90.76	54.55
0.02	−0.1408	0.8893	91.67	54.64
0.40	−0.1365	0.9111	95.14	55.38
0.60	−0.1287	0.9488	104.51	58.17
0.80	−0.1165	1.0055	132.21	68.05
0.90	−0.1079	1.0431	168.80	82.18
0.91	−0.1069	1.0474	174.99	84.60
0.92	−0.1059	1.0517	182.03	87.39
0.93	−0.1049	1.0562	190.14	90.62
0.94	−0.1038	1.0608	199.66	94.45
0.95	−0.1027	1.0656	211.07	99.04
0.96	−0.1016	1.0705	225.43	104.97
0.97	−0.1004	1.0755	244.48	112.94
0.98	−0.0993	1.0808	272.55	124.94
0.99	−0.0983	1.0864	323.50	147.28
1.00	−0.0998	1.0925	593.52	283.05

in Appendix A briefly as follows: Each of these diagrams has one renormalized interaction line which sums up the series of all the polarization bubbles and one bare interaction line. Due to this, if we use the expression of the integrand for each diagram that is being integrated along the imaginary frequency iv, one can separate the regions of the integration as we did for the calculation of the $c_L(\zeta)$ in Appendix A. By doing this, we can keep track of the coefficients of the expansion in r_s of $\epsilon_r(r_s, \zeta)$. Since the diagram has one renormalized interaction line, this gives a dependence on r_s in the integrand inside a logarithm of the dielectric function.

A. Fit equations for the ring diagram

1. *Small* r_s *limit*

For a given value of ζ, we fit the data as a function of r_s in a small region of r_s ($0 < r_s < 1$) to the function

$$\epsilon_r(r_s, \zeta) = c_0 + c_L \ln(r_s) + c_1 r_s + c_2 r_s \ln(r_s), \tag{40}$$

using the exact coefficient c_L as a function of ζ. This fit yields the values of the coefficient $c_0(\zeta)$ given in the first column of Table II for the values of ζ for which we have calculated diagram. We are not going to use the values of the other coefficients obtained this way in our functional; these other coefficients were only necessary in order to extract the correct value of c_0. As explained in the following, we are only going to force the contribution of the ring series to our functional to have the correct c_0 and c_L coefficients in the $r_s \to 0$ limit.

2. *Large* r_s *limit*

For the large r_s limit ($100 < r_s < 1\,000\,000$), we have found that the numerical results for $\epsilon_r(r_s, \zeta)$ can be very accurately fit to the form

$$\epsilon_r(r_s, \zeta) = \frac{e_0}{r_s^{\frac{3}{4}}} + \frac{e_1}{r_s}. \tag{41}$$

We know that at very large r_s values, when the $1/r_s^{3/4}$ term is the dominant term [4], the coefficient e_0 should be $e_0 = -0.803$ Ry as calculated *exactly* in Appendix B. It was also found to be ζ independent. We have verified that, when we fit the results for $r_s > 1000$, e_0 approaches the calculated value. Therefore, we adopt this value of e_0 for our functional for all values of ζ. The values of e_1 found by fitting this large r_s ($r_s > 100$) behavior is given in the second column of Table II for data corresponding to the calculated values of ζ.

3. *Our functional for all values of* r_s

We will need a compact functional form to describe our data for the series of the ring diagrams which satisfy the above discussed small r_s and large r_s behavior, and at the same time it describes accurately our numerical results in the entire region, especially the region of r_s realized in the real materials. We found that the following form accomplishes these requirements:

$$\epsilon_r(r_s, \zeta) = (a_0 + a_1 r_s) \ln\left(1 + \frac{a_2}{r_s^2}\right) + (b_0 + b_1 r_s) \ln\left(1 + \frac{b_2}{r_s^{7/4}}\right), \tag{42}$$

where the coefficients $a_n = a_n(\zeta), b_n = b_n(\zeta)$ $(n = 1, 2, 3)$ are functions of ζ.

The small r_s limit given by Eq. (15) imposes the following constraint on the coefficients:

$$a_0 \ln(a_2) + b_0 \ln(b_2) = c_0, \tag{43}$$

$$2a_0 + \frac{7}{4} b_0 = -c_L, \tag{44}$$

where, for simplicity, we used the notation c_0 simply for $c_0(\zeta)$ and c_L for $c_L(\zeta)$. There are no spurious terms, such as $\sim\sqrt{r_s}$, which exist in the PBE functional in the small r_s limit. The ζ dependence of c_L is analytically known [Eq. (16)].

In the next step of our fitting procedure, we fit our results to the functional form given by Eq. (42) in the range $0 < r_s < 100$ with the constraints given by Eqs. (43) and (44) and the following additional constraints:

$$a_1 a_2 = e_1, \tag{45}$$

$$b_1 b_2 = e_0, \tag{46}$$

where e_1 and e_0 are the known coefficients already discussed and $e_0 = -0.803$ and e_1 is tabulated in the second column of Table II.

For any given value of ζ we fit the data to the form given by Eq. (42). There are six unknowns and the four equations. The other parameters can be expressed in terms of a_2 and b_2

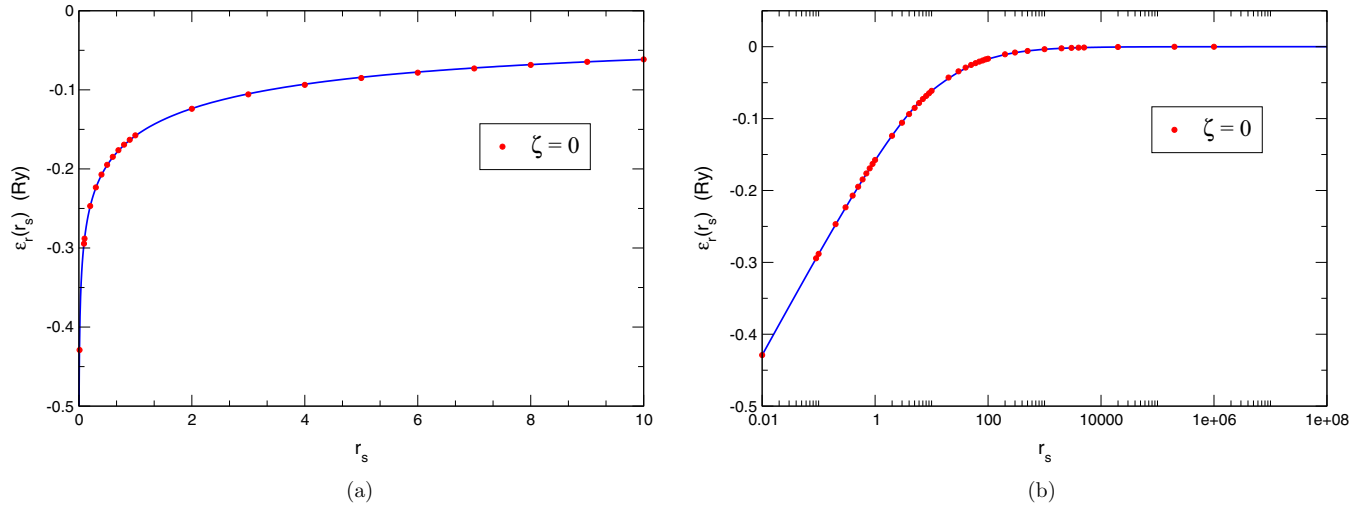

FIG. 11. Fit of the form given by Eq. (42) of our numerical results by numerical integration of the expression given by Eq. (12) for the sum of the ring diagrams. (a) Small r_s region. (b) The entire region.

by solving the above four equations. We find

$$a_0 = -\frac{1}{2}\left[c_L + \frac{7}{4}\frac{2c_0 + c_L \ln(a_2)}{2\ln(b_2) - \frac{7}{4}\ln(a_2)}\right], \tag{47}$$

$$b_0 = \frac{2c_0 + c_L \ln(a_2)}{2\ln(b_2) - \frac{7}{4}\ln(a_2)}, \tag{48}$$

$$a_1 = \frac{e_1}{a_2}, \tag{49}$$

$$b_1 = \frac{e_0}{b_2}. \tag{50}$$

Using these expressions for the coefficients a_0, a_1, b_0, b_1 in terms of a_2 and b_2, we can do a two-parameter fit for each calculated value of ζ. Namely, the same procedure is repeated for any given value of ζ and the the results of the fits are given in Table II.

The quality of the fit to the formula given by Eq. (42) for $\zeta = 0$ is illustrated in Fig. 11(a) for small values of r_s and in Fig. 11(b) for the whole range of r_s. For all other values of ζ the fits are shown in Fig. 12.

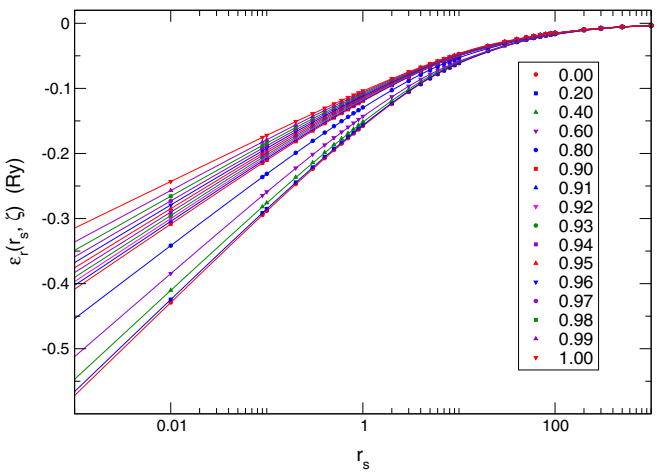

FIG. 12. The data points are the ring-diagram data from Table VIII for different values of ζ and the solid lines are the fit of the ring diagram using the functional given by Eq. (42).

4. *Functional dependence on spin polarization ζ*

Now, we wish to find interpolation formulas to describe the ζ dependence of the coefficients in Table II. First, the values of the constant $c_0(\zeta)$ are plotted in Fig. 13. Notice that the form

$$c_0(\zeta) = \sum_{n=0}^{2} c_{0n}\zeta^{2n} \tag{51}$$

fits the data very well with the exception of the region near $\zeta = 1$ as illustrated in Fig. 13 by the blue dashed line. This behavior near $\zeta = 1$ was first discussed in Ref. [26]. We were able to obtain a reasonable fit in the whole region of ζ using the following interpolation formula:

$$c_0(\zeta) = \sum_{n=0}^{1} c_{0n}\zeta^{2n} + \sum_{n=1}^{3} \bar{c}_{0n}(\chi^n - 2^n), \tag{52}$$

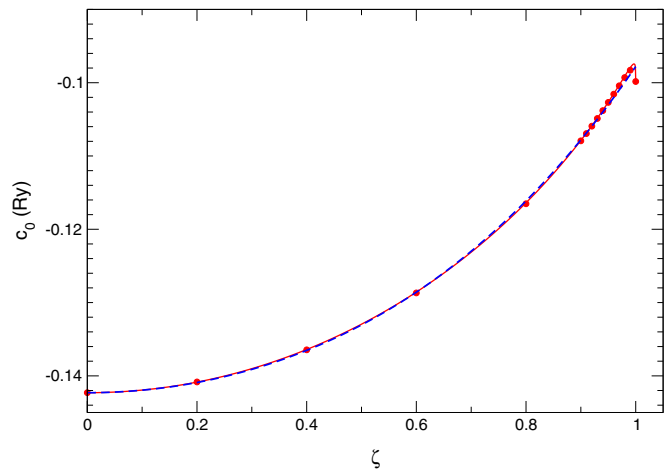

FIG. 13. ζ dependence of the constant c_0 of the functional.

TABLE III. Coefficients for c_0 entering in Eq. (52) (in Ry).

n	0	1	2
c_{0n}	−0.1423	0.0036	0
$\bar{c}_{0n}$	0.1971	−0.0326	−0.0177

where $\chi(\zeta)$ is given by Eq. (17). The reason for the 2^n is because $\chi(0) = 2$, i.e., we forced the fit to the constraint that the value of $c_0(\zeta = 0)$ should be that of Table II, namely, $c_{00} = c_0(0)$. This form captures the singular behavior near $\zeta = 1$ by the fact that the variable χ has a singular dependence on ζ near $\zeta = 1$. The fit is very good and it is given by the red solid line in Fig. 13. The coefficients c_{0n} ($n = 0, 1$) and $\bar{c}_{0n}$ ($n = 1, 2, 3$) are given in Table III.

It is well known [27] that there is an additional constraint linking $\epsilon_r(r_s, \zeta)$ for $\zeta = 0$ and 1:

$$\epsilon_r(r_s, 1) = \tfrac{1}{2}\epsilon_r(r_s', 0), \tag{53}$$

where r_s' is the rescaled Wigner-Seitz radius given by $r_s' = r_s/2^{4/3}$. We did not impose this constraint because we found that our results, given in Appendix E for the ring series, satisfy this relationship for all values of r_s within error bars. The above expression, which leads to the following relationship between $c_0(0)$ and $c_0(1)$,

$$c_0(1) = \frac{1}{2}c_0(0) - \frac{4}{3\pi^2}\ln(2)[1 - \ln(2)], \tag{54}$$

is found to be satisfied within the errors of the fitting procedures (a) in Table II, where the values listed were found by fitting to the small r_s formula given by Eq. (40) and (b) in the results of the fitting procedure to the expression given by Eq. (52), where Eq. (54) was not imposed.

We used the form

$$e_1(\zeta) = \sum_{n=0}^{2} e_{1n}\zeta^{2n} \tag{55}$$

to parametrize the ζ dependence of e_1. We forced the fit to the constraint that the value of $e_1(\zeta = 0)$ is that of Table II, i.e., $e_{10} = e_1(0)$. The other coefficients e_{1n} are given in the second row of Table IV and a graph illustrating the quality of the fit is given in Fig. 14.

The values of the coefficients a_2 and b_2 as a function of ζ are fit to the form

$$a_2 = a_{20} + a_{21}(\chi - 2) + a_{22}\left(\frac{\ln(\chi)}{\chi} - \frac{\ln(2)}{2}\right), \tag{56}$$

$$b_2 = b_{20} + b_{21}(\chi - 2) + b_{22}\left(\frac{\ln(\chi)}{\chi} - \frac{\ln(2)}{2}\right). \tag{57}$$

TABLE IV. Coefficients for e_1 (in Ry), a_2, and b_2 entering in Eq. (57).

n	1	2
e_{1n}	0.1648	0.0432
a_{2n}	192.62	−3956.38
b_{2n}	149.46	−2070.06

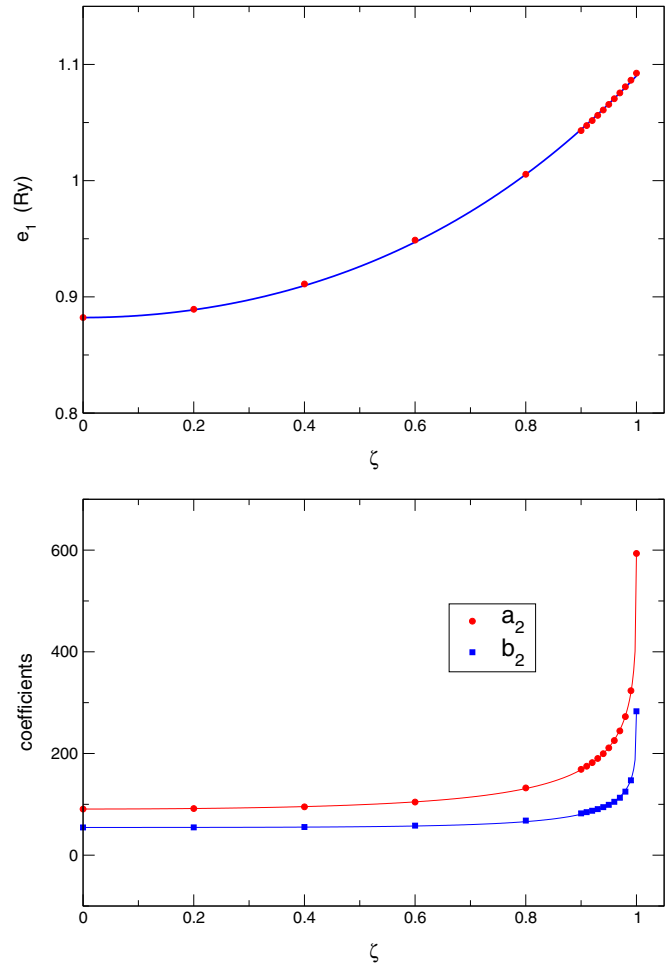

FIG. 14. The data points are the values of Table II and the solid lines are the coefficients of Table IV fitted to the form (55) for e_1 (top) and (57) for a_2 and b_2 (bottom).

Again, we forced the fit to the constraint that $a_{20} = a_2(\zeta = 0)$ and $b_{20} = b_2(\zeta = 0)$ given in Table II determined earlier. The other coefficients are given in the last two rows of Table IV and a graph illustrating the quality of the fit is given in Fig. 14.

B. Fit equations for the kite diagram

We also need to represent the calculated data for the kite-diagram series as a function of r_s and polarization ζ with a functional form which accurately reproduces the Onsager result at the static and $r_s \to 0$ limit and fit accurately the data for all the calculated values of r_s. It would have been nice to have other constraints obtained analytically to impose on the functional form. However, handling analytically the 11-dimensional integral in any limit has turned out to be difficult. Nevertheless, we have found numerically that the kite-diagram series decay as $1/\sqrt{r_s}$ at large values of r_s and we chose a functional form that has this asymptotic behavior. The following form can fit accurately the results for the kite-diagram series:

$$\epsilon_{2b}(r_s) = \frac{a_0}{1 + a_1 r_s} + a_2 r_s \ln\left(1 + \frac{1}{a_3 r_s + a_4 r_s^{3/2}}\right), \tag{58}$$

TABLE V. Coefficients of the fit of the kite diagram for different values of ζ obtained by fitting the data in Table IX.

ζ	a_1	a_2 (Ry)	a_3	a_4
0.0	0.10215	−0.01382	0.46529	0.00364
0.2	0.10876	−0.01317	0.45202	0.00329
0.4	0.10456	−0.01305	0.46978	0.00291
0.6	0.07801	−0.01265	0.4441	0.00277
0.8	0.06266	−0.01023	0.36888	0.00179
0.9	0.05106	−0.00835	0.29562	0.00148
1.0	0.04143	−0.00571	0.19503	0.00088

where to obtain the $r_s \to 0$ limit found by Onsager, we enforce $a_0 = 0.048\,36$ Ry, so this is only a four-parameter fit. Repeating the fit to our results for all the calculated values of ζ, we obtain the values listed in Table V for the values of these four parameters for the calculated values of ζ and the quality of the fit is illustrated in Fig. 15.

We use the following interpolation functional for the ζ dependence of these four coefficients:

$$a_n = \sum_{m=0}^{2} a_{nm}\zeta^{2m} \quad \text{for } n = 1, 2, 3, 4, \tag{59}$$

where we forced the fit to go through the value of each coefficient obtained for $\zeta = 0$ as in the case of the ring-diagram series, i.e., $a_{n0} = a_n(0)$. The other two coefficients a_{n1} and a_{n2} for each value of values of n obtained by fitting the results listed in Table V are given in Table VI.

The quality of the fit for $\zeta = 0$ is as shown in Fig. 16(a) for small r_s values and in Fig. 16(b) for a range of r_s which spans several orders of magnitude. The results for other values of ζ are illustrated in Fig. 17.

IV. COMPARISON OF THE RPAF FUNCTIONAL WITH OTHER FUNCTIONALS

A. Comparison with the PW functional

In Fig. 18 the RPAF functional is compared with the PW functional as a function of r_s for the spin-unpolarized case.

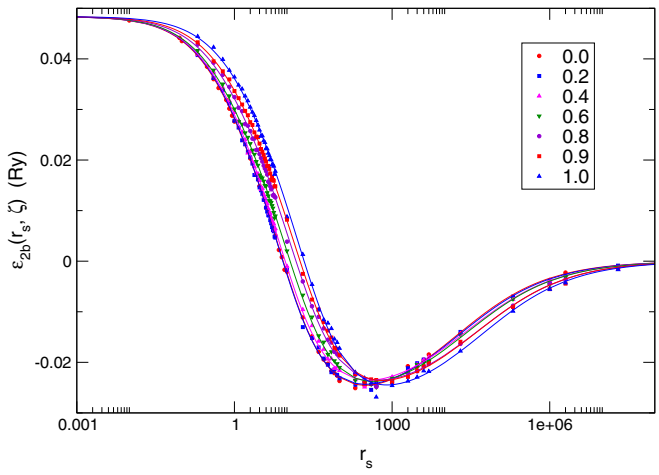

FIG. 15. The data points are the kite-diagram data from Table IX and the solid lines the fit of the kite diagram presented in Eq. (58).

TABLE VI. Coefficients for a_1, a_2, a_3, and a_4 (in Ry) as function of ζ obtained by fitting the kite-diagram data.

$n\backslash m$	1	2
1	−0.05028	−0.01283
2	0.00016	0.00808
3	0.05868	−0.32923
4	−0.00259	−0.00021

We also plot the Monte Carlo results from Ref. [7] for various values of N. Note that the raw data obtained in Ref. [6], i.e., for any given value of N, are not available. Only the $N \to \infty$ "extrapolated" results are provided. For the purpose of the following discussion the N dependence of the results is needed. Nevertheless, the results of Ref. [7] are even more valuable, as they are for larger values of N.

In Fig. 19 we plot the Monte Carlo results from Ref. [7] for various values of N vs $1/N^{\frac{2}{3}}$ as this is the reading term in $N \to \infty$ limit in the forms used in Refs. [6,7,28]. From this figure, it becomes evident that, unless the asymptotic form of the correlation energy per site $\epsilon_c(N)$ for very large N is known, the extrapolation process cannot distinguish between the PW values (blue solid circle at the origin) and the RPAF values (magenta solid circle at the origin). They both seem to be within the error of the extrapolation. Note that the PW functional was obtained by fitting its form to the extrapolation results of Ref. [6], which are for values of N even smaller than the ones used in our Fig. 19. Notice that the N dependence is neither smooth nor monotonic. A nonmonotonic behavior is a clear sign that the results of the finite-N Monte Carlo calculations have not reached the $N \to \infty$ asymptote for a clear and unambiguous $N \to \infty$ extrapolation. Moreover, the formula for extrapolation used in these Monte Carlo studies was not based on any detailed knowledge of the actual form, which is based on the structure of the interaction.

In the low r_s region there is the $\ln(r_s)$ singularity which is obtained within RPA due to the emergence of the infrared cutoff $q_{\rm IR} = \sqrt{2\alpha r_s/\pi}$ (which is proportional to the Thomas-Fermi screening length in units of the Fermi wave vector). However, when N is not infinite there is a second competing emergent cutoff given by

$$q_N = \frac{2\pi\sqrt{3}}{(3\pi^2 N)^{\frac{1}{3}}}, \tag{60}$$

which interferes with the extraction of the well-known $c_L \ln(r_s)$ term given by Eq. (15). Therefore, one has to be in the region where $q_N \ll q_{\rm IR}$ to obtain the asymptotic ($N \to \infty$) value given by Eq. (16). However, for a value of $N \sim 246$ (which is the maximum value calculated in Ref. [6]) the equation $q_{\rm IR} = q_N$ (where one begins to feel the existence of q_N) leads to a value of r_s of the order of unity. Moreover, for larger r_s this modification of the dependence of $\epsilon_c(N)$ on N should cross over to a different one *smoothly* as a function or r_s; therefore, the extrapolation forms discussed in Refs. [6,7,28,29] are not valid for even larger values of r_s. Therefore, one deals with relative large finite-size effects especially for small values of r_s.

In conclusion, the belief that the PW functional is based on results of accurately extrapolated Monte Carlo results is not

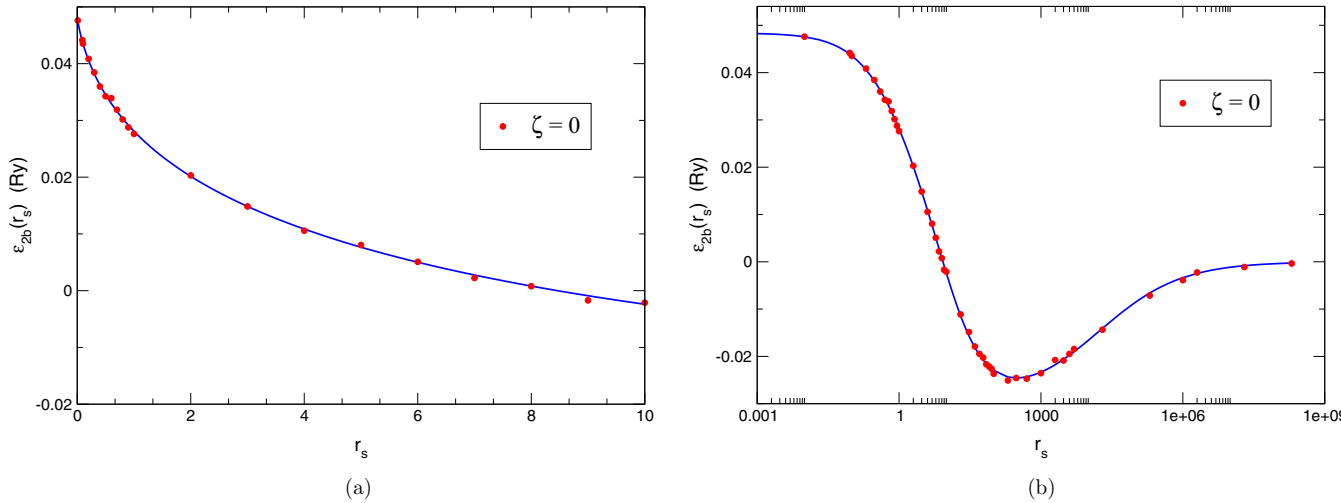

FIG. 16. Fit of the form given by Eq. (58) to our numerical results obtained by Monte Carlo integration of the expressions given by Eqs. (28) and (29) for the kite-diagram series. (a) Small r_s region. (b) The entire region.

quite valid, at least for values of $r_s \simeq 2$ which were used to fit the PW functional.

B. Comparison with SOSEX

In this subsection we compare the results of our method to SOSEX [30], which stands for second-order screened exchange, a computational method used to calculate the correlation energy for the homogeneous electron gas based on the coupled-cluster expansion.

The coupled-cluster expansion method [31–33] specifically solves the time-independent Schrödinger's equation by writing the ground state of the many-electron system as an operator of the form $\hat{R} \equiv e^{-\hat{S}}$ acting on a noninteracting ground state. The ansatz involves the operator $\hat{R}$, which is not unitary, typically applied to the ground-state solution from the Hartree-Fock problem. The exponential contains the so-called "cluster" operator, where the order of the cluster expansion depends on up to what "nth" body operator has been used. The order of the approximation that has been used for the homogeneous electron gas by SOSEX is for $n = 2$, where the cluster operator depends on the combination of two-body and single-particle operators [30]. The focus of this method is to use the ansatz to find the expectation value of the bare Coulomb potential operator $\hat{V}$. By rearranging the terms that reproduce the correlation energy, conveniently, one can isolate a specific normal ordering between the annihilation and creation operators that reproduce the RPA results within a good degree of accuracy. By subtracting this term to the whole expression that contributes to the correlation energy by the RPA, the leftover is what is commonly known as SOSEX.

The SOSEX contribution has a specific normal ordering of the annihilation and creation operators that contributes to the correlation energy. Such rearrangement of operators can be represented as a diagram that has the same topology as

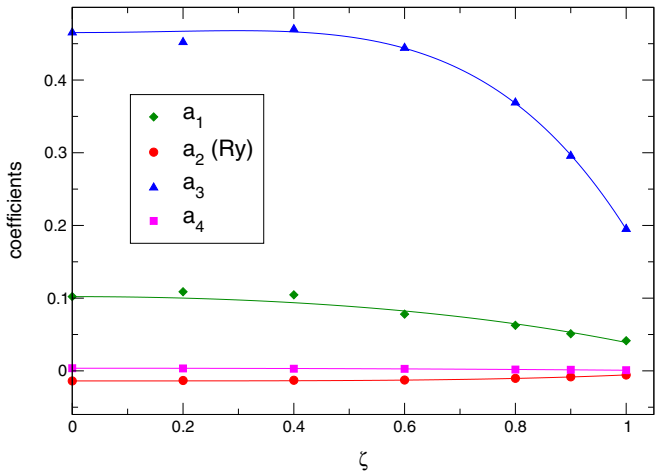

FIG. 17. The data points are the values of Table V and the solid lines are the result of the fit to the form in Eq. (59) for the coefficients of Table VI.

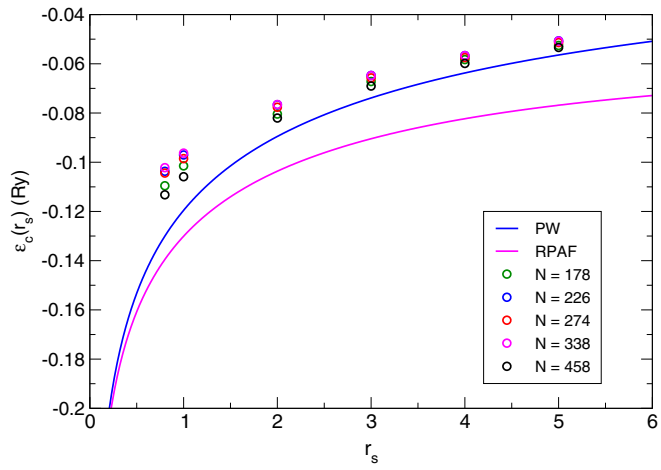

FIG. 18. Comparison of the RPAF functional correlation energy (magenta line) as a function of r_s with the PBE functional (blue line) and the MC results on finite-size lattices.

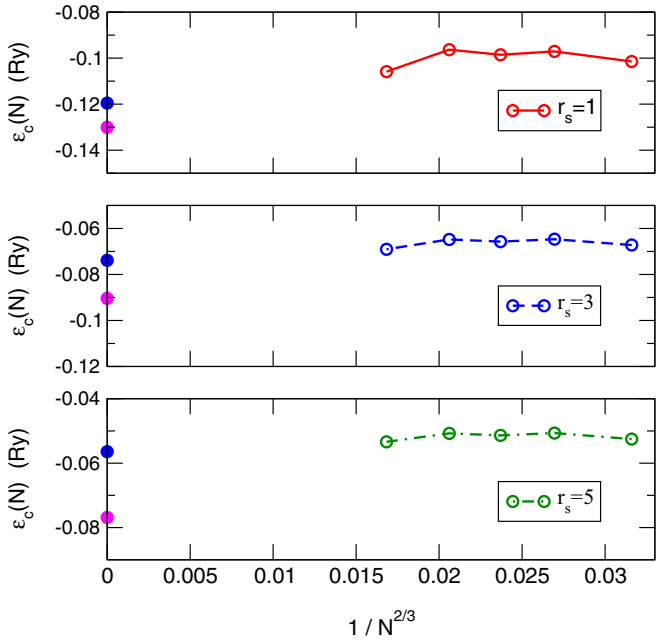

FIG. 19. We plot the correlation energy as calculated by Monte Carlo in Ref. [7] (open circles) for different number of electrons N as a function of $1/N^{\frac{2}{3}}$ for various values of $r_s = 1, 3, 5$. The blue solid circle at the origin is the value for the PW functional, while the magenta is the corresponding value of the RPAF functional.

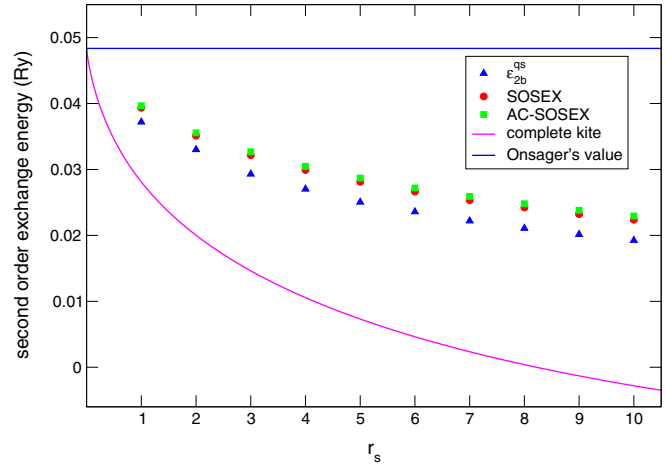

FIG. 20. Comparison between the results of the full-kite-diagram series from Table IX at $\zeta = 0$, the values obtained in the quasistatic limit for the full-kite-diagram series $\epsilon^{\rm qs}_{2b}(r_s, 0)$, Onsager's value, the SOSEX [30], and the AC-SOSEX values.

the full-kite diagram (from Fig. 8), which we calculated in this work. The difference in the approaches for calculating the correlation energy is that the coupled cluster starts from a time-independent perturbation expansion, while in our case we include time-dependent effects. Namely, when calculating the full-kite diagram series, we take into consideration the collective behavior of the screening interaction by performing the frequency integrals. Based on such differences in the approaches, we suspect that the results of the correlation energy between these two approaches should be different.

More specifically, the expression of the full-kite diagram has a total of four integrals that were calculated by using Onsager's constant ϵ^0_{2b} and the correction to the kite diagram, given by the sum of Eqs. (C5) and (C6). When the branch cuts of the dielectric function are ignored, two out of the four integrals remain for the correction to the kite diagram since in the integral of the first term in the brackets of Eq. (C5) all the complex poles are below the real line, while the integral from the second term of the brackets of Eq. (C6), all the complex poles are above the real line. Hence, we think the major disagreement comes from the extra contribution that arises by avoiding the branch cuts from the dielectric function when doing the contour complex integration in the frequency variable, which is ignored in the time-independent approach (SOSEX). To test this explanation for the disagreement, we carry out an approximation to the frequency variable of the dielectric function by setting it to zero, and compare the results with SOSEX.

If we set $\omega = 0$ in the expression for the kite-diagram series and carry out all frequency integrals (of the free-interacting Green's functions) we obtain the following expression:

$$\epsilon^{\rm qs}_{2b}(r_s, 0) = \frac{3}{8\pi^5}\int_0^1 d\lambda \int_{k\leqslant 1} d^3k \int_{q_2\leqslant 1} d^3q_2 \times \int d^3q_1 \frac{\lambda\Theta(|\vec{q}_1+\vec{q}_2|-1)\Theta(|\vec{k}+\vec{q}_1|-1)}{\epsilon_\lambda(q_1,0)q_1^2\left[q_1^2+(\vec{q}_2+\vec{k})\cdot\vec{q}_1\right]|\vec{k}+\vec{q}_2+\vec{q}_1|^2}, \quad (61)$$

where the superscript "qs" stands for quasistatic.

In Fig. 20, we have made a comparison between the results of the full-kite diagram at $\zeta = 0$ by using the data reported in Table IX and the SOSEX data given in Ref. [30]. There is a large numerical discrepancy between these two results, as expected since the two approaches differ in a very important way as discussed earlier. The results obtained in the quasistatic limit [Eq. (61)] and Onsager's value are shown to compare the SOSEX results obtained by Freeman [30]. Notice that the results obtained by SOSEX are close to the results obtained using the additional (and unnecessary) approximation given by Eq. (61) to the full kite-diagram series.

Additionally, the data obtained from Eq. (61) by Monte Carlo integration was fitted to the equation given by Eq. (39). The value of the coefficient found for the $r_s \ln r_s$ term in the long-wavelength limit is given by 0.005 72 Ry, which almost agrees with the C_1 value of 0.006 41 Ry, found for PW contribution (i.e., the difference of PW from the sum of the ring-diagram series) by the same fitting procedure reported in Sec. II E. The numerical results of the correlation energy obtained by SOSEX almost agree with the correlation energy from the PW functional. This means that the hypothetical coefficient of the $r_s \ln r_s$ obtained from the SOSEX data should almost agree with the $C1$ obtained through the PW functional reported in Table I. Therefore, while a subset of the terms that occur in the coupled-cluster expansion agrees well with the RPA results obtained by Hedin [23], there is a major disagreement with the C_1 value reported by Ref. [25].

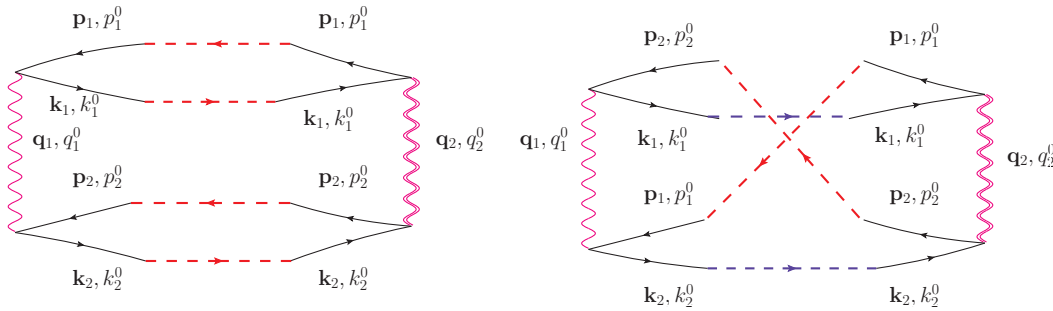

FIG. 21. Diagrammatic illustration that the kite-diagram series (right) can be obtained from the ring-diagram series (left) by exchanging the frequency-momentum indices of two of the fermionic propagators.

Therefore, the SOSEX contribution to the correlation energy corresponds to approximating the dielectric function with its frequency-independent limit. However, this is a poor approximation to this important response function because it ignores the retardation effects [24] which characterize the response of the electronic system to not only external time-dependent electric fields, but more importantly to the effective interaction between electrons inside the jellium system. When one ignores such effects, this interaction gives the Thomas-Fermi result, which fails to produce the Friedel oscillations.

AC-SOSEX [34–36] is a method which attempts to include the frequency dependence in the second-order exchange diagram contribution to the correlation energy using the adiabatic connection-dissipation formalism (ACFD). AC-SOSEX has been used on several materials [35] and the homogeneous electron gas [36].

Within the ACFD formalism, the RPA part of the correlation energy, E_c^{RPA}, has been calculated and can be written as

$$E_c^{\mathrm{RPA}} = -\frac{1}{2}\int_{-\infty}^{\infty}\frac{dv}{2\pi}\sum_{ijab} W_{ij}^{ab}(iv)F_i^a(iv)F_j^b(iv)V_{ab}^{ij}, \quad (62)$$

where i, j (a, b) correspond to the quantum numbers of the occupied (unoccupied) states. V_{ab}^{ij} [$W_{ij}^{ab}(iv)$] are the matrix element of the bare Coulomb (coupling-strength averaged RPA-renormalized) interaction written in the particle- and hole-state basis and $F_i^a(iv)$ is the particle and hole propagator as defined in Ref. [35] (see also Ref. [36]).

This expression yields the correct expression for the ring-diagram series in the homogeneous electron gas problem. Within the AC-SOSEX method, the second-order exchange diagram is obtained from Eq. (62) by doing an interchange between the occupied state indices in the V_{ab}^{ij} term and by picking up an extra minus sign as a global factor, as explained in Refs. [35,36].

This is motivated by the fact that the ring-diagram series and the kite-diagram series are related by a similar exchange when one writes their expressions using the Feynman rules of the many-body time-dependent perturbation approach. This is demonstrated in Fig. 21. Namely, the diagram on the right (kite series) can be obtained from the diagram on the left (ring series) by simply exchanging indices of the two fermionic lines, which in this case represent two four-momenta (momentum and frequency) labels of the bare interaction term. Notice, however, that these are 4-momenta indices, which include the frequency indices. However, in order to obtain the RPA result given by Eq. (62), two of these frequency integrations have been carried out. As a result, starting from this reduced equation the other two frequency indices are gone and, thus, there is no way to carry out the required exchange of the full 4-vector indices in order to obtain the kite diagrams starting from the RPA.

The fact that AC-SOSEX and the corresponding diagrams obtained by many-body perturbation are different was also argued in Ref. [36]. As illustrated in Fig. 20 the results of the AC-SOSEX are very close to the SOSEX case and substantially different from our kite-diagram contribution.

V. BENCHMARKING OUR FUNCTIONAL

In order to assess the accuracy of our functional, we modified the QUANTUM ESPRESSO v7.2 package [14] to include our functional as an option and we carried out DFT calculations within the local density approximation (LDA) for the same entire list of crystalline materials given in Refs. [15–17] where the performance of various other functionals was evaluated.

The set of solids used in Ref. [15] containing 60 crystals was used to compare the predicted lattice constant and bulk modulus of the RPAF functional with the popular Perdew-Wang (PW) LDA functional [5]. The experimental lattice constants were obtained from Ref. [15] and the bulk moduli from Ref. [16]. Pseudopotentials were generated for the PW and RPAF functionals using the ld1.x in QUANTUM ESPRESSO with the pslibrary1.0.0 library of inputs [37]. A $10 \times 10 \times 10$ Monkhorst-Pack mesh was used for the reciprocal lattice space for all the crystals. For the energy cutoff required for convergence, we found that, depending on the material, a range from 40 Ry up to 140 Ry was good enough. Self-consistent calculations were done for nine different lattice constants, four above and four below the equilibrium lattice constant, with a step of 0.01 Bohr radius. Afterward, the nine points were fitted using the third-order Birch-Murnaghan equation of state using the ev.x tool in QUANTUM ESPRESSO to obtain the equilibrium lattice constant and bulk modulus.

The Perdew, Burke, and Ernzerhof (PBE) functional [3] shares the same local part with the PW [5] functional, i.e., PBE is PW plus the correction based on the generalized gradient approximation (GGA). The GGA is an additional

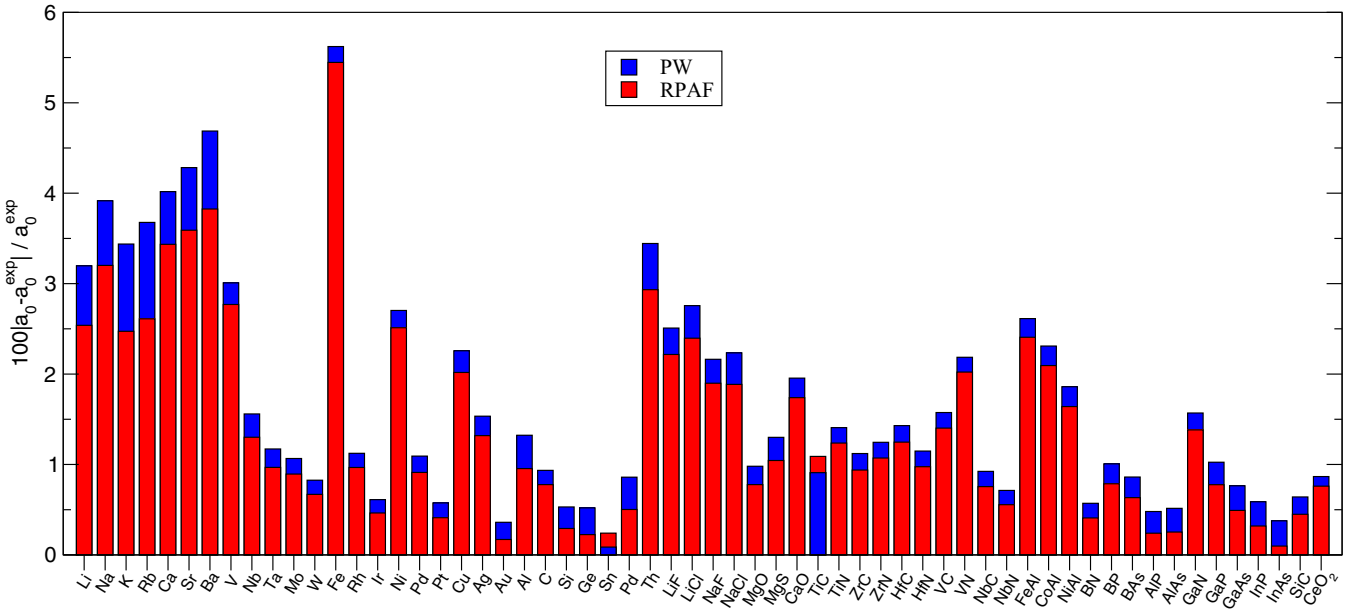

FIG. 22. Relative errors of equilibrium lattice constants (a_0) of the 60 crystals listed in Ref. [15] using the PW functional (blue) and the RPAF functional presented in this work (red). The calculations were done in QUANTUM ESPRESSO. The values are listed in Appendix E.

feature included in the PBE functional, which can be adopted or not, namely, it has a different and independent goal from the question of the local part of the functional. We are mindful that the focus of this paper is precisely the local part of the functional. Therefore, when we try to assess the accuracy of our functional we compare it only to the PW functional since the PBE and PW share the same local part.

The results are compared with the PW functional in the bar graph of Fig. 22 for the lattice constants and in Fig. 23 for the bulk moduli and the precise numerical values are given in the tables of Appendix E. Our functional, which is represented by the red color bars in both figures, are systematically better than the results obtained with the PW functional.

We did not extend these LDA calculations to include GGA corrections to compare with the PBE functional because such an extension, albeit useful, will not provide a direct benchmarking of the functional proposed here. Namely, this proposal only affects the local part of the density functional. How to go beyond LDA is a useful future direction of our work.

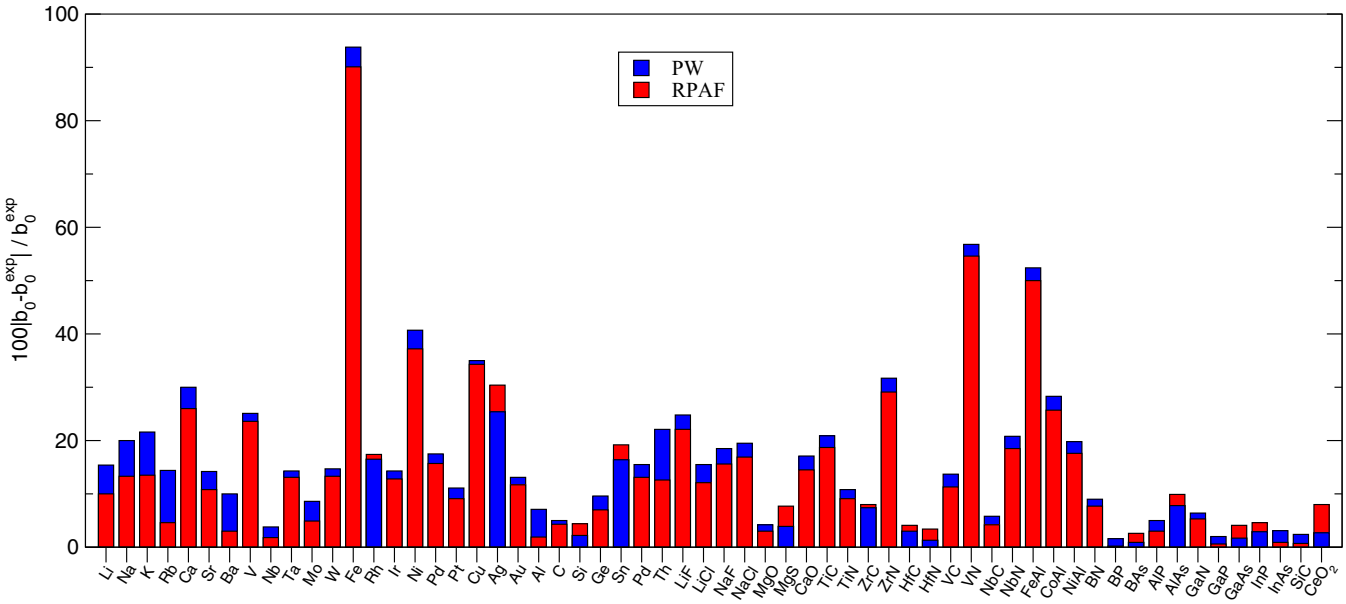

FIG. 23. Relative errors of equilibrium bulk moduli (B_0) of 60 crystals listed in Ref. [15] using the PW functional (blue) and the RPAF functional presented in this work (red). The values are listed in Appendix E.

VI. CONCLUSIONS

The local part of most available functionals is fit to QMC calculations which are inaccurate and feel strong finite-size effects, especially when the electron gas is spin polarized.

We have argued that the perturbation expansion in an RPA-renormalized interaction line not only removes the infinities introduced by the bare Coulomb interaction but it also allows a fast convergence with respect to the number of RPA-renormalized interaction lines. Therefore, we should expect such an expansion to approach the correct functional for a broad range of value of r_s due to the screening effects without having to go to a high order in this expansion.

We computed the r_s and spin-polarization dependence of the correlation energy to the leading order in the RPA-renormalized interaction, including the frequency dependence of the dielectric function. This leads to a functional of the density and of spin polarization expressed in an analytic form. We modified the QUANTUM ESPRESSO implementation of DFT to include our functional as one option and we benchmarked our functional on a list of materials selected and used in Refs. [15–17]. We demonstrated that the functional proposed here yields in general better relaxed lattice constants and bulk moduli (Figs. 22 and 23) than the local part of the popular functionals PW [5] (and, therefore, PBE [3] because they share the same local functional).

For completeness, in Appendix D we studied the fate of ferromagnetism of the uniform electron fluid as implied by our functional. Our findings are in qualitative agreement with other functionals derived from QMC [6] that the fully polarized electron gas becomes favorable for values of r_s well outside the region accessible by crystalline solids and outside the region of validity of our expansion.

This work introduces a systematic order-by-order approach in the number of RPA-renormalized interaction lines, which can be improved by including the next-order correction. This stands in contrast to the previously introduced functionals, which are based on *ad hoc* procedure and, thus, produce questionable results. The next-order correction within this method, although cumbersome, is achievable and will be our future project.

ACKNOWLEDGMENTS

This work was supported by the U.S. National Science Foundation under Grant No. NSF-DMR-2110814. We thank M. Langley who wrote a code to independently calculate the integrals given by Eqs. (28) and (29) to verify the results of our calculation.

APPENDIX A: SMALL r_s LIMIT OF THE RING-DIAGRAM SERIES

In this Appendix, we present the calculation of the coefficient of the $\ln(r_s)$ corresponding to the ring-diagram series for the spin-polarized electron gas. The sum of all Goldstone diagrams illustrated in Fig. 4 relies on the computation of the polarization tensor $\Pi^0_\sigma(q^\mu)$, which is obtained from doing the integral given in Eq. (8).

The calculation of the ring-diagram series $E_r(r_s,\zeta)$ relies on finding an expression for the self-energy $\Sigma^r_\sigma(q,q^0)$:

$$\Sigma^r_\sigma(q^\mu,\lambda) = \int \frac{d^4p}{(2\pi)^4\hbar^2}\int \frac{d^4k}{(2\pi)^4}\frac{[\lambda V_0(q)]^2}{\epsilon_\lambda(q,q_0)} \times G^0_\sigma(k^\mu - q^\mu)\sum_{\sigma'} G^0_{\sigma'}(p^\mu + q^\mu)G^0_{\sigma'}(p^\mu), \tag{A1}$$

which by using this expression in Eq. (5) we obtain an expression for the contribution to the ground-state energy given by the ring-diagram series. One can rewrite the expression of the integrated ring-diagram series into a more compact form as a function of the polarization tensor:

$$E_r(r_s,\zeta) = \frac{i\hbar V}{2}\int_0^1 d\lambda \int \frac{d^4q}{(2\pi)^4}\frac{\lambda[1-\epsilon(q,q^0)]^2}{\epsilon_\lambda(q,q^0)}, \tag{A2}$$

where $\epsilon_\lambda(q,q^0)$ is the dielectric function given by Eq. (7) with the coupling constant rescaled $e^2 \to \lambda e^2$. A useful change of variable can be performed at the integrand to convert the physical variables into dimensionless parameters as follows: $q \to k_F\kappa$, $q^0 \to \hbar k_F^2 \nu/m$. By doing this, the number of particles can be factored out and we can express the contribution to the ground-state energy in terms of the ring-diagram series per particle $\epsilon_r(r_s,\zeta)$, as seen in Eq. (10). After performing the integral over the λ, we obtain the expression given in Eq. (11).

Instead of integrating the frequency variable ν along the real line, we can exploit Cauchy's theorem. If we take the same path we used to calculate the $E_{2b}(r_s,\zeta)$ diagram, we can avoid the branch cuts from the logarithmic terms of the dielectric function which causes the integration over ν along the real line mapped into an integral along the imaginary axis of the complex plane. The parametrization of the new line integral is given by Eq. (12), where we identify that the term in the argument of the logarithm is the dielectric function $\epsilon(k_F\kappa, i\hbar k_F^2\nu/m)$:

$$\epsilon\left(k_F\kappa, i\frac{\hbar k_F^2\nu}{m}\right) = 1 + \frac{\alpha r_s}{\pi\kappa^2}\sum_{\sigma=\pm} x_\sigma(\zeta) g\left(\frac{\kappa}{x_\sigma(\zeta)}, \frac{i\nu}{x_\sigma^2(\zeta)}\right), \tag{A3}$$

where g is the function of the Lindhard function given by Eq. (14), which was derived by doing the high-dimensional integral given in Eq. (8) at imaginary frequency.

By exploiting the fact that the integrand of $\epsilon_r(r_s,\zeta)$ is an even function in ν, the expression picks up a factor of 2, and by performing the change of variable $x = \nu/q$ and integrating along the solid angle from the three-dimensional integral, we obtain Eq. (12).

This integral is not trivial to calculate analytically, but to make the integral more tractable when we separate the interval of integration into three different regions: $q \in [0, q_{\rm IR}] \cup [q_{\rm IR}, q_c] \cup [q_c, \infty)$, where $q_c \ll 1$ and $q_{\rm IR}$ is proportional to $r_s^{\frac{1}{2}}$, which gives the notion of an infrared cutoff for the screened interaction potential which arises from the dielectric function of the material in RPA. In the first region, the integration does not yield a $\ln(r_s)$ term, but rather contributions to the higher-order terms in r_s, while the integral along the third region for q yields a contribution to the constant term for the ring-diagram series. We focus only on the second

region of integration since it yields the coefficient of the $\ln(r_s)$ term, whose contribution to the ring-diagram series is called $\epsilon_{r,2}(r_s,\zeta)$. In $q \in [q_{IR}, q_c]$, we can do a Taylor expansion in terms of $(\alpha r_s)/(\pi q^2)$ at the level of the logarithm term of the integrand from Eq. (12) up to the second order, where in such small q region the Lindhard function can be approximated as

$$g\left(\frac{q}{x_\sigma(\zeta)}, i\frac{xq}{x_\sigma^2(\zeta)}\right) = 2\left[1 - \frac{x}{x_\sigma}\tan^{-1}\left(\frac{x_\sigma}{x}\right)\right] - \frac{q^2 x_\sigma^2}{6\left(x^2 + x_\sigma^2\right)^2}. \tag{A4}$$

The first term in parentheses of Eq. (A4) yields the $\ln(r_s)$ term when used in the second region of integration in the ring diagram per particle $\epsilon_{r,2}(r_s,\zeta)$. By ignoring the q^2 term in Eq. (A4), we obtain the following expression for $\epsilon_{r,2}(r_s,\zeta)$:

$$\epsilon_{r,2}(r_s,\zeta) = \frac{3}{\pi^3}\ln\left(\frac{q_{\rm IR}}{q_c}\right)\sum_{i=1}^{3} I_i(\zeta), \tag{A5}$$

with $q_{\rm IR} = \gamma_2 r_s^{\frac{1}{2}}$, for some constant γ_2, and the integrals are along the ratio x are $I_1(\zeta)$, $I_2(\zeta)$, and $I_3(\zeta)$, which are given by the following expressions:

$$I_1(\zeta) = \int_0^\infty dx\, h_\uparrow^2(x,\zeta) = \frac{\pi}{3}(\zeta_+)[1 - \ln(2)], \tag{A6}$$

$$I_2(\zeta) = \int_0^\infty dx\, h_\downarrow^2(x,\zeta) = \frac{\pi}{3}(\zeta_-)[1 - \ln(2)], \tag{A7}$$

$$I_3(\zeta) = 2\int_0^\infty dx\, h_\uparrow(x,\zeta) h_\downarrow(x,\zeta) = \frac{\pi}{3}\left[\frac{\zeta_+^{\frac{1}{3}}\zeta_-^{\frac{1}{3}}\chi}{2} + \frac{1}{6}ln\left(\frac{\zeta_+^{\zeta_+}\zeta_-^{\zeta_-}}{\chi^6}\right)\right], \tag{A8}$$

where $\zeta_\pm = 1 \pm \zeta$, χ was defined in Eq. (17) and the function $h_\sigma(x,\zeta)$ is defined as follows:

$$h_\sigma(x,\zeta) = x_\sigma(\zeta) - x\ \arctan\left(\frac{x_\sigma(\zeta)}{x}\right). \tag{A9}$$

The three integrals have been calculated by using a simple change of variable $y = 1/x$ and then integrating along the complex plane by avoiding the branch cuts that come from the logarithmic terms that come from integration by parts. By using these results we obtain the $\ln(r_s)$ dependence of the ring-diagram series per particle for small r_s:

$$\epsilon_r(r_s,\zeta) = c_L(\zeta)\ln(r_s) + c_0, \tag{A10}$$

where $c_L(\zeta)$ is the coefficient of the $\ln(r_s)$ term we previously discussed in Eq. (16).

APPENDIX B: LARGE r_s DEPENDENCE OF THE SUM OF THE RING DIAGRAMS

In this Appendix, we show how to obtain the asymptotic behavior of $\epsilon_r(r_s,\zeta)$ for large r_s. The change of variable $x = v/\kappa$ was done in Eq. (14) to study the large r_s region. After this, it is convenient to do the following change of variables: $\kappa = 2Q$ and after this mathematical step, we did the transformation $x = yQ$.

According to the behavior of the Lindhard function at imaginary frequency, as Q and y variables increase, this function decreases to values less than 1. For the purpose of making the integral expression of $\epsilon_r(r_s,\zeta)$ tractable given in Eq. (12), we will find the region such as the condition for $\tilde{\Pi}(2Q, Qy, \zeta, r_s) < 1$ is satisfied. By considering that this Lindhard function yields its maximum value when both variables Q and y are zero $[g(0,0) = 2]$, and the fact that $\tilde{\Pi}(2Q, yQ, \zeta, r_s)$ is proportional to the Wigner-Seitz radius r_s but inversely proportional to Q^2, we have that $\tilde{\Pi}(2Q, yQ, \zeta, r_s)$ is less than unity only at some relatively large value of Q. We can expect that such value of Q that satisfies the condition for $\tilde{\Pi}(2Q, yQ, \zeta, r_s)$ will depend on the variable y due to the behavior of the function to decrease in value as the y variable increases.

At the large Q limit, the logarithm and the arc tangent functions in the expression of the Lindhard function can easily be expanded in powers of $1/Q$. We obtain

$$g\left(\frac{2Q}{x_\sigma(\zeta)}, i\frac{2yQ^2}{x_\sigma^2(\zeta)}\right) \overset{k\to\infty}{\approx} \frac{2x_\sigma^2(\zeta)}{3Q^2(1+y^2)}. \tag{B1}$$

By replacing this approximated expression of the Lindhard function in Eq. (13) we obtain the approximated expression of $\Pi(2Q, yQ, \zeta, r_s)$ to find the value of Q that guarantees that this function is less than unity. The approximated expression is

$$\tilde{\Pi}(2Q, yQ, \zeta, r_s) \overset{Q\to\infty}{\approx} \frac{\alpha r_s}{3\pi Q^4(1+y^2)}, \tag{B2}$$

where the condition $\tilde{\Pi}(2Q, yQ, \zeta, r_s) < 1$ is only achieved if the inequality $Q > \overset{*}{k}(r_s, y)$, where $\overset{*}{k}(r_s, y)$ is given by

$$\overset{*}{k}(r_s, y) = \left(\frac{\alpha r_s}{3\pi(1+y^2)}\right)^{\frac{1}{4}}. \tag{B3}$$

We can now start approximating the integral expression of $\epsilon_r(r_s,\zeta)$ by separating the region of integration into two parts on the Q variable:

$$\epsilon_r(r_s,\zeta) = \epsilon_{r1}(r_s,\zeta) + \epsilon_{r2}(r_s,\zeta), \tag{B4}$$

where the first term integrates over $y \in [0,\infty)$ and the region of integration $Q \in (0, \overset{*}{k}(r_s, y)]$, which we call region 1. The second term is the contribution to $\epsilon_r(r_s,\zeta)$ in the second region of integration, which integrates on y half of the real line, and Q is integrated into $Q \in [\overset{*}{k}(r_s, y), \infty)$.

The integral in the second region was calculated by Perdew, where it relies on using the simplified expression of $\tilde{\Pi}(2Q, yQ, \zeta, r_s)$ we found in Eq. (B2) to calculate all of the required integrals.

In the second region of integration, the integral is simple to calculate due to the condition on the function $\tilde{\Pi}(2Q, Qy, \zeta, r_s) < 1$, which makes it possible to do a Taylor expansion on the logarithm term of the integrand in small values of $\tilde{\Pi}(2Q, Qy, \zeta, r_s)$. To obtain the accurate contribution to the term that captures the asymptotic region of $\epsilon_r(r_s,\zeta)$ in the low-density regime, we must take into consideration all orders of expansion of the logarithm term. From such expansion, we

have so far

$$\epsilon_{r2}(r_s,\zeta) \approx \frac{-24}{\pi(\alpha r_s)^2}\int_0^\infty dy \int_{\overset{*}{k}(r_s,y)}^\infty dQ\, Q^4 \sum_{n=2}^\infty S_n, \tag{B5}$$

where the term S_n in the series is given by

$$S_n = \frac{(-1)^n[\tilde{\Pi}(2Q, yQ, \zeta, r_s)]^n}{n}. \tag{B6}$$

By using the expression given in Eq. (B2) in the integral above, the integral over Q is simple to do, so we are left with an integral over y:

$$\epsilon_{r2}(r_s,\zeta) = -\frac{24}{\delta}\sum_{n=2}^\infty \frac{(-1)^n}{n(4n-5)}\int_0^\infty dy \frac{1}{(1+y^2)^{\frac{5}{4}}}, \tag{B7}$$

where $\delta \equiv 3^{\frac{5}{4}}\pi^{\frac{9}{4}}(\alpha r_s)^{\frac{3}{4}}$ and the sum over n and the integral over the y variable have been calculated with Wolfram *Mathematica*, which yield

$$M_1 = \sum_{n=2}^\infty \frac{(-1)^n}{n(4n-5)} \approx 0.133\,628, \tag{B8}$$

$$M_2 = \int_0^\infty \frac{dy}{(1+y^2)^{\frac{5}{4}}} = \frac{2\sqrt{\pi}\Gamma\left(\frac{3}{4}\right)}{\Gamma\left(\frac{1}{4}\right)}. \tag{B9}$$

By using these two results we obtain the asymptotic behavior of the ring diagram, where region 2 only has a partial contribution to the coefficient of the term $r_s^{-3/4}$. We obtained

$$\epsilon_{r2}(r_s,\zeta) \overset{r_s\to\infty}{\approx} -\frac{2\Xi M_1}{r_s^{\frac{3}{4}}} \approx -\frac{0.120\,772}{r_s^{\frac{3}{4}}}, \tag{B10}$$

where Ξ is a numerical factor that we will express in most of our calculations in this subsection, which is given by the following expression:

$$\Xi \equiv \frac{24\Gamma\left(\frac{3}{4}\right)}{\sqrt{\pi}(3\pi)^{\frac{5}{4}}\Gamma\left(\frac{1}{4}\right)\alpha^{\frac{3}{4}}}. \tag{B11}$$

In the first region of integration, we exploit the fact that the following condition for the function $\tilde{\Pi}(2Q, yQ, \zeta, r_s) \geqslant 1$ is satisfied. In the first region of integration of $\epsilon_r(r_s,\zeta)$, we expand the logarithm terms in the integrand in powers of $1/[\tilde{\Pi}(2Q, Qy, \zeta, r_s)]$. Three main integrals have to be calculated in the first region:

$$\epsilon_{r1}(r_s,\zeta) = \epsilon^1_{r1}(r_s,\zeta) + \epsilon^2_{r1}(r_s,\zeta) + \epsilon^3_{r1}(r_s,\zeta), \tag{B12}$$

where each of these terms are given by the following integrals:

$$\epsilon^1_{r1}(r_s,\zeta) = \frac{\gamma_3}{r_s^2}\int_0^\infty dy \int_0^{\overset{*}{k}} dQ\, Q^4 \ln(\tilde{\Pi}), \tag{B13}$$

$$\epsilon^2_{r1}(r_s,\zeta) = \frac{\gamma_3}{r_s^2}\int_0^\infty dy \int_0^{\overset{*}{k}} dQ\, Q^4 \ln\left(1+\frac{1}{\tilde{\Pi}}\right), \tag{B14}$$

$$\epsilon^3_{r1}(r_s,\zeta) = -\frac{\gamma_3}{r_s^2}\int_0^\infty dy \int_0^{\overset{*}{k}} dQ\, Q^4 \tilde{\Pi}, \tag{B15}$$

where $\tilde{\Pi} = \tilde{\Pi}(2Q, Qy, \zeta, r_s)$ due to the change of variables done in previous steps $\gamma_3 = 24/(\pi\alpha^2)$.

The first integral can be expressed as

$$\epsilon^1_{r1}(r_s,\zeta) = \frac{24}{\pi(\alpha r_s)^2}\int_0^\infty dy \int_0^{\overset{*}{k}(r_s,y)} dQ\, Q^4 \times\left[\ln\left(\frac{\alpha r_s}{4\pi}\right) - 2\ln(Q) + \ln\left(\sum_\sigma x_\sigma(\zeta) g\left(\frac{2Q}{x_\sigma(\zeta)}, \frac{2yQ^2}{x^2_\sigma(\zeta)}\right)\right)\right], \tag{B16}$$

which can be further broken into a sum of three terms $\epsilon^1_{r1\alpha}(r_s,\zeta)$ (where $\alpha = 1, 2, 3$ correspond to the three terms in the brackets), where the first and second terms can be integrated easily, which yields

$$\epsilon^1_{r11}(r_s,\zeta) = \frac{2\Xi\ln\left(\frac{\alpha r_s}{4\pi}\right)}{5r_s^{\frac{3}{4}}}, \tag{B17}$$

$$\epsilon^1_{r12}(r_s,\zeta) = \frac{\delta_2}{r_s^{\frac{3}{4}}}\left[4 + \frac{\delta_3}{2\Gamma\left(\frac{3}{4}\right)} - 5\ln\left(\frac{\alpha r_s}{3\pi}\right)\right], \tag{B18}$$

where $\delta_2 = \Xi/25$, $\delta_3 = 5M_3\Gamma(\frac{1}{4})/\sqrt{\pi}$, and M_3 is the following integral:

$$\int_0^\infty dy \frac{\ln(1+y^2)}{(1+y^2)^{\frac{5}{4}}} = 1.028\,49. \tag{B19}$$

For the last term in Eq. (B16), which we call $\epsilon^1_{r13}(r_s,\zeta)$, we did a change of variable to remove the r_s and y dependence in the limit of integration by using the transformation $Q = \overset{*}{k}(r_s, y)p$. In such integrand, we can do an expansion of the Lindhard function in the large r_s limit. After doing this transformation, we obtain the following:

$$g\left(\frac{2Q}{x_\sigma(\zeta)}, i\frac{2Q^2y}{x^2_\sigma(\zeta)}\right) = \frac{2x^2_\sigma(3\pi)^{\frac{1}{2}}}{3p^2(\alpha r_s)^{\frac{1}{2}}(1+y^2)^{\frac{1}{2}}}. \tag{B20}$$

By replacing such expression in the last term inside of the brackets in Eq. (B16), we obtain

$$\epsilon^1_{r13}(r_s,\zeta) \approx \frac{\delta_2}{r_s^{\frac{3}{4}}}\left[4 - \frac{\delta_3}{2\Gamma\left(\frac{3}{4}\right)} - 5\ln\left(\frac{3\alpha r_s}{16\pi}\right)\right]. \tag{B21}$$

By summing the terms from Eqs. (B17), (B18), and (B21) we obtain the contribution to the coefficient of the $r_s^{-3/4}$:

$$\epsilon_{r11}(r_s,\zeta) = \frac{192\Gamma(\frac{3}{4})}{25\sqrt{\pi}\alpha^{\frac{3}{4}}(3\pi)^{\frac{5}{4}}\Gamma\left(\frac{1}{4}\right)r_s^{\frac{3}{4}}}. \tag{B22}$$

The calculation of $\epsilon_{r12}(r_s,\zeta)$ relies on using the same change of variable that we used to calculate $\epsilon^1_{r13}(r_s,\zeta)$ to make the limits of integration to be independent of r_s and y. By expanding the logarithm and keeping track of all orders of

expansion we obtain

$$\epsilon_{r12}(r_s,\zeta) \approx \frac{48\Gamma\left(\frac{3}{4}\right)M_4}{\sqrt{\pi}\alpha^{\frac{3}{4}}(3\pi)^{\frac{5}{4}}\Gamma\left(\frac{1}{4}\right)r_s^{\frac{3}{4}}}, \tag{B23}$$

where M_4 is a series that we calculated on Wolfram *Mathematica*, which yields

$$M_4 = \sum_{n=1}^{\infty} \frac{(-1)^{n+1}}{n(4n+5)} \approx 0.085\,05. \tag{B24}$$

Similarly as done for $\epsilon_{r12}(r_s,\zeta)$, we can calculate the last integral in the first region of integration:

$$\epsilon_{r13}(r_s,\zeta) \approx -\frac{16\Gamma\left(\frac{3}{4}\right)}{\pi^{\frac{3}{2}}\alpha^{\frac{3}{4}}(3\pi)^{\frac{1}{4}}\Gamma\left(\frac{1}{4}\right)r_s^{\frac{3}{4}}}. \tag{B25}$$

By summing the three terms in Eq. (B12) we obtain the leading term for the sum of ring diagrams in region 1:

$$\epsilon_{r1} \approx -\frac{0.682\,313\,4}{r_s^{\frac{3}{4}}}, \tag{B26}$$

and by adding such a term to the result we have obtained in region 2 given by Eq. (B10), we obtain that the leading term of the integral is of the power form of $r_s^{-3/4}$ and its coefficient is given below:

$$\epsilon_r(r_s,\zeta) \approx -\frac{0.8031}{r_s^{\frac{3}{4}}}, \tag{B27}$$

which agrees with our numerical results from our fitted region for large values of r_s within errors.

APPENDIX C: CALCULATION OF THE KITE DIAGRAM

We avoid the issue of the "sign" problem, by doing a set of transformations to the wave vector and frequency variable which will also simplify the expression and reduce the dimension of the integral given in Eq. (23). This is easily done by isolating one of the frequency variables from the rest in the argument of the dielectric function at the Goldstone diagram given by Eq. (23). This allows the possibility of doing the other two frequency integrals by using Cauchy's residue theorem and thus avoiding taking into consideration the branch cuts that arise from the logarithmic terms in the expression of the dielectric function. After doing the two frequency integral variables k^0 and q_2^0, we obtain the sum of two terms $\Delta_1[n_\uparrow,n_\downarrow]$ and $\Delta_2[n_\uparrow,n_\downarrow]$ given by the following integral expressions:

$$\Delta E_{2b}^{\mathrm{RPA}}[n_\uparrow,n_\downarrow] = \Delta_1[n_\uparrow,n_\downarrow] + \Delta_2[n_\uparrow,n_\downarrow], \tag{C1}$$

where the two main contributions that we have so far for the correction of the kite diagram are given by the following:

$$\begin{aligned}\Delta_1[n_\uparrow,n_\downarrow] = &-\frac{iV}{2\hbar(2\pi)^{10}}\sum_{\{\sigma\}=\pm}\int_0^1 d\lambda\int d^4q_1\int d^3q_2\int d^3k\frac{\lambda^2V_0(\vec{k}-\vec{q}_1-\vec{q}_2)V_0^2(q_1)}{\epsilon_\lambda\left(q_1,q_1^0\right)\left(q_1^0+\omega_{\vec{q}_2,\sigma}-\omega_{\vec{q}_1+\vec{q}_2,\sigma}+i\eta\right)}\\ &\times\Pi^0\left(q_1,q_1^0\right)\Theta(k_{F\sigma}-q_2)\Theta(|\vec{q}_1+\vec{q}_2|-k_{F\sigma})\\ &\times\left[\frac{\Theta(k-k_{F\sigma})\Theta(k_{F\sigma}-|\vec{k}-\vec{q}_1|)}{q_1^0+\omega_{\vec{k}-\vec{q}_1,\sigma}-\omega_{\vec{k},\sigma}+i\eta}-\frac{\Theta(k_{F\sigma}-k)\Theta(|\vec{k}-\vec{q}_1|-k_{F\sigma})}{q_1^0+\omega_{\vec{k}-\vec{q}_1,\sigma}-\omega_{\vec{k},\sigma}-i\eta}\right],\end{aligned} \tag{C2}$$

$$\begin{aligned}\Delta_2[n_\uparrow,n_\downarrow] = &\frac{iV}{2\hbar(2\pi)^{10}}\sum_{\{\sigma\}=\pm}\int_0^1 d\lambda\int d^4q_1\int d^3q_2\int d^3k\frac{\lambda^2V_0(\vec{k}-\vec{q}_1-\vec{q}_2)V_0^2(q_1)}{\epsilon_\lambda\left(q_1,q_1^0\right)\left(q_1^0+\omega_{\vec{q}_2,\sigma}-\omega_{\vec{q}_1+\vec{q}_2,\sigma}-i\eta\right)}\\ &\times\Pi^0\left(q_1,q_1^0\right)\Theta(q_2-k_{F\sigma})\Theta(k_{F\sigma}-|\vec{q}_1+\vec{q}_2|)\\ &\times\left[\frac{\Theta(k-k_{F\sigma})\Theta(k_{F\sigma}-|\vec{k}-\vec{q}_1|)}{q_1^0+\omega_{\vec{k}-\vec{q}_1,\sigma}-\omega_{\vec{k},\sigma}+i\eta}-\frac{\Theta(k_{F\sigma}-k)\Theta(|\vec{k}-\vec{q}_1|-k_{F\sigma})}{q_1^0+\omega_{\vec{k}-\vec{q}_1,\sigma}-\omega_{\vec{k},\sigma}-i\eta}\right],\end{aligned} \tag{C3}$$

where the frequencies $\omega_{\vec{k}\sigma}$ are related to the energy dispersion of the electrons as $\omega_{\vec{k}\sigma}=\epsilon_{\vec{k}\sigma}/\hbar$ and $\Pi^0(q_1,q_1^0)$ is the spin trace of the polarization tensor.

In the integral expression of $\Delta_2[n_\uparrow,n_\downarrow]$, we can do the transformations $\vec{q}_2\to\vec{q}_2-\vec{q}_1$ followed by $\vec{q}_1\to-\vec{q}_1$. These momentum transformations are what allow a common product of Heaviside functions for both $\Delta_1[n_\uparrow,n_\downarrow]$ and $\Delta_2[n_\uparrow,n_\downarrow]$. We obtain

$$\begin{aligned}\Delta_2[n_\uparrow,n_\downarrow] = &\frac{iV}{2\hbar(2\pi)^{10}}\sum_{\{\sigma\}=\pm}\int_0^1 d\lambda\int d^4q_1\int d^3q_2\int d^3k\frac{\lambda^2V_0(\vec{k}-\vec{q}_2)V_0^2(q_1)}{\epsilon_\lambda\left(q_1,q_1^0\right)\left(q_1^0+\omega_{\vec{q}_1+\vec{q}_2,\sigma}-\omega_{\vec{q}_2,\sigma}-i\eta\right)}\\ &\times\Pi^0\left(q_1,q_1^0\right)\Theta(k_{F\sigma}-q_2)\Theta(|\vec{q}_1+\vec{q}_2|-k_{F\sigma})\\ &\times\left[\frac{\Theta(k-k_{F\sigma})\Theta(k_{F\sigma}-|\vec{k}+\vec{q}_1|)}{q_1^0+\omega_{\vec{k}+\vec{q}_1,\sigma}-\omega_{\vec{k},\sigma}+i\eta}-\frac{\Theta(k_{F\sigma}-k)\Theta(|\vec{k}+\vec{q}_1|-k_{F\sigma})}{q_1^0+\omega_{\vec{k}+\vec{q}_1,\sigma}-\omega_{\vec{k},\sigma}-i\eta}\right].\end{aligned} \tag{C4}$$

A sequence of wave-vector transformations has been done for both expressions given by Eqs. (C2) and (C4) to simplify them and to find a common product of Heaviside functions since this makes easier the computation of these two 11-dimensional

integrals by the MC method. For $\Delta_1[n_\uparrow, n_\downarrow]$ the sequence of wave-vector transformations goes as follows: First, on both terms of Eq. (C2) flip the parity of wave vector $\vec{k} \to -\vec{k}$. After this, on the resulting integral expression, transform the first of the two 11-dimensional integrals by the following translation on the wave vector: $\vec{k} \to \vec{k} - \vec{q}_1$. Lastly, on the first integrand do the following two parity transformations: $\vec{q}_2 \to -\vec{q}_2$ and $\vec{q}_1 \to -\vec{q}_1$. This yields the following simplified expression for $\Delta_1[n_\uparrow, n_\downarrow]$:

$$\Delta_1[n_\uparrow, n_\downarrow] = -\frac{iV}{2\hbar(2\pi)^{10}} \sum_{\{\sigma\}=\pm} \int_0^1 d\lambda \int d^4q_1 \int_{q_2 \leqslant k_{F\sigma}} d^3q_2 \int_{k<k_{F\sigma}} d^3k \frac{\lambda^2 V_0^2(q_1)\Pi^0(\vec{q}_1, q_1^0)}{\epsilon_\lambda(q_1, q_1^0)(q_1^0 + \omega_{\vec{q}_2,\sigma} - \omega_{\vec{q}_1+\vec{q}_2,\sigma} + i\eta)}$$
$$\times \Theta(|\vec{q}_1 + \vec{q}_2| - k_{F\sigma})\Theta(|\vec{k} + \vec{q}_1| - k_{F\sigma}) \left[\frac{V_0(\vec{k} - \vec{q}_2)}{(q_1^0 + \omega_{\vec{k},\sigma} - \omega_{\vec{k}+\vec{q}_1,\sigma} + i\eta)} - \frac{V_0(\vec{k} + \vec{q}_1 + \vec{q}_2)}{(q_1^0 + \omega_{\vec{k}+\vec{q}_1,\sigma} - \omega_{\vec{k},\sigma} - i\eta)} \right]. \quad \text{(C5)}$$

The expression of $\Delta_2[n_\uparrow, n_\downarrow]$ can be simplified in a similar way as done for $\Delta_1[n_\uparrow, n_\downarrow]$ by a sequence of transformations of wave vectors. For the first term of the integrand in Eq. (C4), we do the translation $\vec{k} \to \vec{k} - \vec{q}_1$. To the integrand resulting from the previous step, the following transformation has to be performed, $\vec{k} \to -\vec{k}$, which leads to the following expression:

$$\Delta_2[n_\uparrow, n_\downarrow] = \frac{iV}{2\hbar(2\pi)^{10}} \sum_{\{\sigma\}=\pm} \int_0^1 d\lambda \int d^4q_1 \int_{q_2 \leqslant k_{F\sigma}} d^3q_2 \int_{k<k_{F\sigma}} d^3k \frac{\lambda^2 V_0^2(q_1)\Pi^0(\vec{q}_1, q_1^0)}{\epsilon_\lambda(q_1, q_1^0)(q_1^0 + \omega_{\vec{q}_1+\vec{q}_2,\sigma} - \omega_{\vec{q}_2,\sigma} - i\eta)}$$
$$\times \Theta(|\vec{q}_1 + \vec{q}_2| - k_{F\sigma})\Theta(|\vec{k} + \vec{q}_1| - k_{F\sigma}) \left[\frac{V_0(\vec{k} + \vec{q}_1 + \vec{q}_2)}{(q_1^0 + \omega_{\vec{k},\sigma} - \omega_{\vec{k}+\vec{q}_1,\sigma} + i\eta)} - \frac{V_0(\vec{k} - \vec{q}_2)}{(q_1^0 + \omega_{\vec{k}+\vec{q}_1,\sigma} - \omega_{\vec{k},\sigma} - i\eta)} \right]. \quad \text{(C6)}$$

In order to simplify the computation of the correction of the kite diagram in RPA, instead of only integrating q_1^0 over the real line, we can instead exploit Cauchy's theorem. We can choose to integrate along a contour path in the complex plane. The contour path C can be separated into four path integrals: C_1, C_2, C_3, C_4. The path C_1 corresponds to the line integral over the real line, C_2 would correspond to the quarter of the circle on the first quadrant of the complex plane with counterclockwise orientation for a radius that tends to infinity, where its contribution to the complex path integral is zero. Path C_3 is the downward-oriented line integral along the imaginary line, while C_4 corresponds to a quarter of a circle path on the third quadrant of the complex plane with clockwise orientation, where its contribution to the complex path integral is also zero when taking the radius of the circular path to ∞. Due to the constraints given by the Heavisides, the complex poles in the expressions given by Eqs. (C5) and (C6) can only be on the second or fourth quadrant of the complex plane. Since none of the complex poles are enclosed by the contour complex path, this means that the integration along the real line can be directly mapped into the integration along the imaginary axis. After doing this and exploiting the fact that the polarization tensor is an even function in frequency q_1^0, we obtain the following expression:

$$\Delta E_{2b}^{\mathrm{RPA}}[n_\uparrow, n_\downarrow] = -\frac{V}{\hbar(2\pi)^{10}} \sum_{\{\sigma\}=\pm} \int_0^1 d\lambda \int_{k<k_{F\sigma}} d^3k \int_{q_2 \leqslant k_{F\sigma}} d^3q_2 \int d^3q_1 \int_{-\infty}^{\infty} d\nu \frac{\lambda^2 [V_0(q_1)]^2}{\epsilon_\lambda(q_1, i\nu))\left[\nu + \left(\omega_{\vec{k}+\vec{q}_1,\sigma} - \omega_{k,\sigma}\right)i\right]}$$
$$\times \Pi_\sigma^0(q_1, i\nu)\Theta(|\vec{k} + \vec{q}_1| - k_{F\sigma})\Theta(|\vec{q}_1 + \vec{q}_2| - k_{F\sigma})$$
$$\times \left[\frac{V_0(\vec{k} - \vec{q}_1)}{[\nu + (\omega_{\vec{q}_1+\vec{q}_2,\sigma} - \omega_{\vec{q}_2,\sigma})i]} - \frac{V_0(\vec{k} + \vec{q}_1 + \vec{q}_2)}{[\nu + (\omega_{\vec{q}_2,\sigma} - \omega_{\vec{q}_1+\vec{q}_2,\sigma})i]} \right]. \quad \text{(C7)}$$

The fact that the polarization tensor is completely real makes it easier to compute using the stochastic integration technique. From Eq. (C7) and by doing the variable transformation $\vec{k} \to k_{F\sigma}\vec{k}$, $\vec{q}_1 \to k_{F\sigma}\vec{q}_1$, $\vec{q}_2 \to k_{F\sigma}\vec{q}_2$, and $\nu \to \hbar k_{F\sigma}^2 \nu/m$, we can extract the units from the expression of the integrand. Also, the correction to the exchange energy per particle $\Delta\epsilon_{2b}[n_\uparrow, n_\downarrow]$ from the kite-diagram series (in Ry) can be further simplified by a doing a simple variable transformation such as $\nu = a(\vec{q}_1, \vec{q}_2)\tan(u)$ and $\nu = a(\vec{q}_1, \vec{k})\tan(u)$, where $a(\vec{q}_1, \vec{q}_2)$ is related to the difference between the energy dispersions given by the expression shown in Eq. (31). The kite-diagram correction term per particle (in Ry) given from the correction that arises from the renormalized interaction line yields two final results we have in Eqs. (28) and (29) that we discussed in the kite-diagram section.

APPENDIX D: FERROMAGNETISM

The magnetic response and the magnetic phase diagram of the correlated electron fluid within RPA or otherwise has a long history [38–40] (see also Ref. [41] and references therein). Here we wish to use our derived functional to ask the question of the stability of the unpolarized phase against the fully spin-polarized one. Some time ago [27], it was found that, if one considers the contribution to the total energy, the kinetic and the exchange term, and only the ring-series term in the correlation energy, there is a value of r_s close to the "physical" region where the fully polarized electron gas becomes energetically more stable than the unpolarized one. However, this turns out to be caused by the approximations used to obtain an estimate for the contribution of the ring series. As shown in Fig. 24(a) the dashed black and dashed red

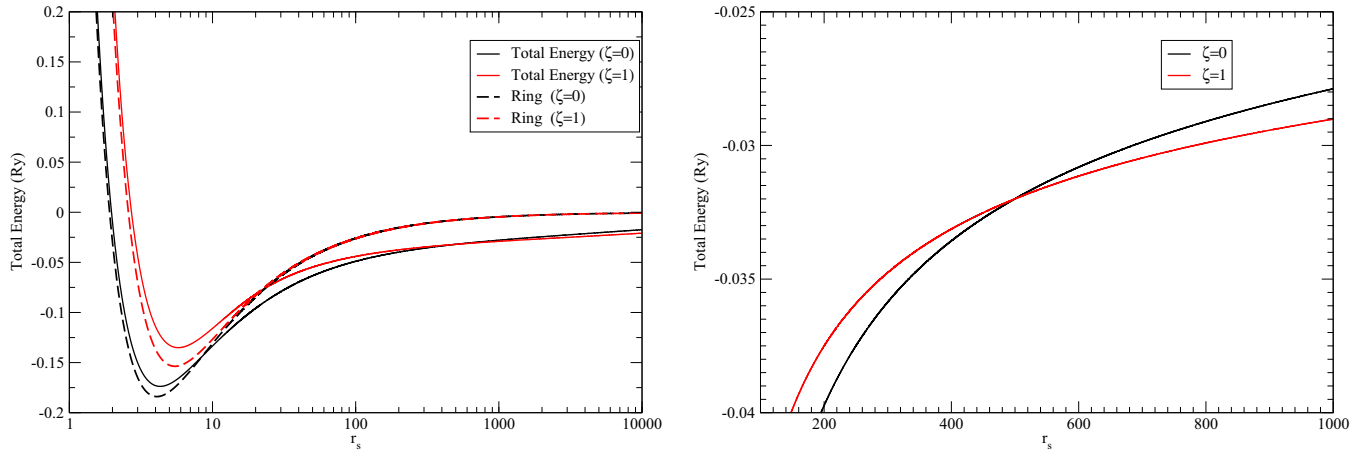

FIG. 24. (a) Comparison of the total energy for $\zeta = 0$ and 1. The solid lines are the total energy which includes the contribution of the kite-diagram series, while the dashed lines do not. (b) A zoom-in of the region where there is a crossing between the energy of the fully polarized with that of the unpolarized.

lines correspond to the total energy when only the ring series is included in the correlation energy for $\zeta = 0$ and 1, respectively. The polarized fluid becomes marginally energetically favorable against the unpolarized for $r_s > 70$ (as also found in Ref. [41], although the energy difference even at $r_s = 100$ is of the order of 10^{-4} Ry which is not comparable with the exchange energy in Fe, for example). However, when we include the contribution of the kite-diagram series, we obtain the solid black ($\zeta = 0$) and solid red ($\zeta = 1$) lines. There is a very large value of r_s of the order of 500, where as illustrated in the zoomed-in Fig. 24(b) the polarized becomes more stable. The energy difference between the fully polarized and the unpolarized electron fluid is sizable in the physical region and it is about the same with or without the contribution of the kite-diagram series. This is in qualitative agreement with other functionals derived from QMC [6,8] that the fully polarized electron gas becomes favorable for values of r_s well outside the "physical" region.

APPENDIX E: TABLES OF NUMERICAL RESULTS

In this Appendix we give tables of various results (Tables VII–IX) discussed in the main part of the paper. The captions explain the content of each table.

TABLE VII. *Results of the DFT calculations*. Equilibrium lattice constants a_0 (Å) and bulk modulus B_0 (GPa) of the 60 crystals listed in Ref. [15]. The solid Strukturbericht symbols are in parentheses and used for the crystals as follows: fcc (A1), bcc (A2), diamond (A4), rocksalt (B1), CsCl (B2), zinc-blende (B3), and fluorite (C1). The statistics reported at the end of the table are mean error (me), mean absolute error (mae), mean relative error (mre), mean absolute relative error (mare), variance, and relative variance. The experimental bulk moduli for most crystals were obtained from Ref. [16], with Pb [42], HfC [43], BAs [17], and CeO_2 [44].

	a_0			B_0				a_0			B_0		
Crystal	PW	RPAF	Expt.	PW	RPAF	Expt.	Crystal	PW	RPAF	Expt.	PW	RPAF	Expt.
Li (A2)	3.366	3.389	3.477	15.0	14.3	13.0	NaF (B1)	4.509	4.521	4.609	60.9	59.4	51.4
Na (A2)	4.060	4.090	4.225	9.0	8.5	7.5	NaCl (B1)	5.470	5.489	5.595	31.8	31.1	26.6
K (A2)	5.045	5.096	5.225	4.5	4.2	3.7	MgO (B1)	4.166	4.174	4.207	171.9	169.9	165
Rb (A2)	5.380	5.439	5.585	3.5	3.2	3.1	MgS (B1)	5.134	5.148	5.202	82.0	85.0	78.9
Ca (A1)	5.341	5.374	5.565	19.5	18.9	15	CaO (B1)	4.709	4.719	4.803	128.8	126.0	110
Sr (A1)	5.789	5.831	6.048	13.7	13.3	12	TiC (B1)	4.268	4.276	4.23	281.6	276.5	233
Ba (A2)	4.772	4.815	5.007	11.0	10.3	10	TiN (B1)	4.179	4.187	4.239	319.0	314.3	288
V (A2)	2.937	2.944	3.028	202.7	200.2	162	ZrC (B1)	4.643	4.652	4.696	245.3	243.7	265
Nb (A2)	3.245	3.253	3.296	176.5	173.0	170	ZrN (B1)	4.528	4.536	4.585	283.2	277.6	215
Ta (A2)	3.262	3.269	3.301	221.7	219.5	194	HfC (B1)	4.572	4.580	4.638	261.9	259.0	270
Mo (A2)	3.110	3.116	3.144	295.5	285.3	272	HfN (B1)	4.468	4.476	4.52	302.0	295.6	306
W (A2)	3.136	3.141	3.162	339.4	335.5	296	VC (B1)	4.094	4.102	4.16	344.4	337.3	303
Fe (A2)	2.700	2.705	2.861	323.6	317.5	167	VN (B1)	4.050	4.057	4.141	365.4	360.2	233
Rh (A1)	3.755	3.761	3.798	313.4	315.8	269	NbC (B1)	4.429	4.436	4.47	333.3	328.1	315
Ir (A1)	3.812	3.817	3.835	405.9	400.3	355	NbN (B1)	4.361	4.368	4.392	352.7	345.9	292
Ni (A1)	3.421	3.428	3.516	258.9	252.4	184	FeAl (B2)	2.814	2.819	2.889	207.2	204.0	136
Pd (A1)	3.839	3.846	3.881	229.1	225.6	195	CoAl (B2)	2.795	2.801	2.861	207.8	203.7	162
Pt (A1)	3.893	3.900	3.916	307.7	302.2	277	NiAl (B2)	2.833	2.840	2.887	186.9	183.4	156
Cu (A1)	3.522	3.530	3.603	179.6	178.6	133	BN (B3)	3.586	3.592	3.607	402.2	397.4	369
Ag (A1)	4.007	4.015	4.069	136.7	142.1	109	BP (B3)	4.492	4.502	4.538	175.8	172.6	173
Au (A1)	4.050	4.058	4.065	188.8	186.5	167	BAs (B3)	4.736	4.747	4.777	146.7	144.1	148
Al (A1)	3.979	3.994	4.032	78.2	74.4	73	AlP (B3)	5.434	5.447	5.46	90.3	88.6	86
C (A4)	3.534	3.539	3.567	465.2	462.1	443	AlAs (B3)	5.629	5.644	5.658	75.6	73.9	82
Si (A4)	5.401	5.414	5.43	97.0	94.8	99.2	GaN (B3)	4.460	4.468	4.531	202.2	200.1	190
Ge (A4)	5.623	5.639	5.652	68.5	70.5	75.8	GaP (B3)	5.392	5.406	5.448	89.8	88.5	88
Sn (A4)	6.476	6.498	6.482	44.3	42.8	53	GaAs (B3)	5.605	5.620	5.648	74.3	72.5	75.6
Pb (A1)	4.874	4.891	4.916	52.9	51.8	45.8	InP (B3)	5.832	5.847	5.866	69.9	68.7	72
Th (A1)	4.899	4.925	5.074	70.8	50.7	58	InAs (B3)	6.031	6.048	6.054	59.8	58.5	58
LiF (B1)	3.909	3.921	4.01	87.1	85.2	69.8	SiC (B3)	4.330	4.338	4.358	230.5	226.5	225
LiCl (B1)	4.965	4.984	5.106	40.9	39.7	35.4	CeO2 (C1)	5.364	5.370	5.411	214.0	202.5	220

	a_0		B_0	
	PW	RPAF	PW	RPAF
me	−0.072	−0.059	21.6	18.6
mae	0.074	0.061	23.9	22.1
mre (%)	−1.654	−1.363	14.1	11.3
mare (%)	1.684	1.407	16.0	14.2
variance	0.0088	0.0061	1468.4	1298.3
relative variance	0.0004	0.0003	0.050	0.043

TABLE VIII. Numerical results for the series of the ring-diagram data (in mRy) generated using adaptive quadrature integration method for many values of ζ and r_s covering the small r_s region, the large r_s region, and the physical region where materials are realized.

$r_s\backslash\zeta$	0.00	0.20	0.40	0.60	0.80	0.90	0.91	0.92	0.93	0.94	0.95	0.96	0.97	0.98	0.99	1.00
0.01	−429.0	−424.4	−410.2	−384.4	−341.6	−308.3	−304.2	−299.8	−295.2	−290.3	−285.0	−279.2	−272.9	−265.7	−256.9	−243.1
0.09	−294.5	−291.4	−281.8	−264.5	−236.1	−214.5	−211.8	−209.0	−206.1	−203.0	−199.6	−196.0	−192.1	−187.7	−182.6	−175.3
0.1	−288.1	−285.1	−275.7	−258.9	−231.2	−210.1	−207.5	−204.8	−201.9	−198.9	−195.6	−192.1	−188.3	−184.1	−179.1	−172.1
0.2	−247.0	−244.4	−236.5	−222.2	−199.0	−181.4	−179.3	−177.1	−174.7	−172.2	−169.6	−166.7	−163.6	−160.2	−156.3	−151.0
0.3	−223.5	−221.2	−214.1	−201.3	−180.6	−165.1	−163.2	−161.2	−159.2	−157.0	−154.7	−152.2	−149.5	−146.6	−143.2	−138.8
0.4	−207.2	−205.1	−198.5	−186.8	−167.9	−153.7	−152.0	−150.2	−148.4	−146.4	−144.3	−142.1	−139.7	−137.1	−134.1	−130.3
0.5	−194.7	−192.7	−186.6	−175.7	−158.1	−145.1	−143.5	−141.9	−140.1	−138.3	−136.4	−134.4	−132.2	−129.8	−127.1	−123.7
0.6	−184.7	−182.8	−177.1	−166.9	−150.4	−138.1	−136.6	−135.1	−133.5	−131.8	−130.1	−128.2	−126.2	−124.0	−121.5	−118.4
0.7	−176.4	−174.7	−169.2	−159.5	−143.9	−132.3	−130.9	−129.5	−128.0	−126.4	−124.8	−123.0	−121.1	−119.1	−116.8	−113.9
0.8	−169.3	−167.6	−162.4	−153.2	−138.3	−127.4	−126.1	−124.7	−123.3	−121.8	−120.3	−118.6	−116.8	−114.9	−112.7	−110.1
0.9	−163.1	−161.5	−156.5	−147.7	−133.5	−123.1	−121.8	−120.5	−119.2	−117.8	−116.3	−114.7	−113.1	−111.2	−109.2	−106.8
1	−157.6	−156.1	−151.3	−142.8	−129.2	−119.2	−118.1	−116.8	−115.6	−114.2	−112.8	−111.3	−109.7	−108.0	−106.1	−103.8
2	−123.9	−122.7	−119.2	−112.8	−102.9	−95.4	−94.6	−93.7	−92.8	−91.9	−90.9	−89.9	−88.8	−87.6	−86.3	−84.8
3	−105.7	−104.7	−101.8	−96.6	−88.5	−82.6	−82.0	−81.3	−80.6	−79.8	−79.1	−78.3	−77.4	−76.5	−75.5	−74.4
4	−93.7	−92.9	−90.4	−86.0	−79.1	−74.1	−73.6	−73.0	−72.4	−71.8	−71.1	−70.5	−69.8	−69.0	−68.2	−67.3
5	−85.0	−84.3	−82.1	−78.2	−72.2	−67.9	−67.4	−66.9	−66.4	−65.9	−65.3	−64.7	−64.1	−63.5	−62.8	−62.0
6	−78.3	−77.6	−75.7	−72.2	−66.8	−63.0	−62.6	−62.2	−61.7	−61.2	−60.7	−60.2	−59.7	−59.1	−58.5	−57.8
7	−72.9	−72.3	−70.5	−67.3	−62.5	−59.1	−58.7	−58.3	−57.9	−57.5	−57.0	−56.6	−56.1	−55.6	−55.0	−54.4
8	−68.4	−67.9	−66.2	−63.3	−58.9	−55.8	−55.4	−55.1	−54.7	−54.3	−53.9	−53.5	−53.1	−52.6	−52.1	−51.6
9	−64.6	−64.1	−62.6	−59.9	−55.8	−53.0	−52.6	−52.3	−52.0	−51.6	−51.2	−50.9	−50.5	−50.1	−49.6	−49.1
10	−61.3	−60.9	−59.5	−57.0	−53.2	−50.5	−50.2	−49.9	−49.6	−49.3	−48.9	−48.6	−48.2	−47.8	−47.4	−47.0
20	−42.8	−42.5	−41.6	−40.1	−37.9	−36.4	−36.2	−36.0	−35.8	−35.6	−35.4	−35.2	−35.0	−34.8	−34.6	−34.3
30	−34.1	−33.9	−33.3	−32.2	−30.6	−29.5	−29.4	−29.3	−29.2	−29.0	−28.9	−28.7	−28.6	−28.4	−28.3	−28.1
40	−28.9	−28.8	−28.3	−27.4	−26.2	−25.3	−25.2	−25.1	−25.0	−24.9	−24.8	−24.7	−24.6	−24.5	−24.3	−24.2
50	−25.4	−25.2	−24.8	−24.1	−23.1	−22.4	−22.3	−22.2	−22.2	−22.1	−22.0	−21.9	−21.8	−21.7	−21.6	−21.5
60	−22.7	−22.6	−22.3	−21.7	−20.8	−20.2	−20.1	−20.1	−20.0	−19.9	−19.9	−19.8	−19.7	−19.6	−19.5	−19.4
70	−20.7	−20.6	−20.3	−19.8	−19.0	−18.5	−18.4	−18.4	−18.3	−18.3	−18.2	−18.1	−18.1	−18.0	−17.9	−17.8
80	−19.1	−19.0	−18.7	−18.3	−17.6	−17.1	−17.1	−17.0	−17.0	−16.9	−16.9	−16.8	−16.7	−16.7	−16.6	−16.5
90	−17.7	−17.7	−17.4	−17.0	−16.4	−16.0	−15.9	−15.9	−15.8	−15.8	−15.7	−15.7	−15.6	−15.6	−15.5	−15.4
100	−16.6	−16.5	−16.3	−15.9	−15.4	−15.0	−15.0	−14.9	−14.9	−14.8	−14.8	−14.7	−14.7	−14.6	−14.6	−14.5
200	−10.7	−10.6	−10.5	−10.3	−10.0	−9.8	−9.8	−9.8	−9.8	−9.7	−9.7	−9.7	−9.7	−9.6	−9.6	−9.6
300	−8.2	−8.1	−8.1	−7.9	−7.7	−7.6	−7.6	−7.6	−7.6	−7.5	−7.5	−7.5	−7.5	−7.5	−7.5	−7.4
500	−5.8	−5.8	−5.7	−5.7	−5.5	−5.5	−5.5	−5.4	−5.4	−5.4	−5.4	−5.4	−5.4	−5.4	−5.4	−5.4
1000	−3.6	−3.6	−3.6	−3.5	−3.5	−3.4	−3.4	−3.4	−3.4	−3.4	−3.4	−3.4	−3.4	−3.4	−3.4	−3.4
2000	−2.2	−2.2	−2.2	−2.2	−2.2	−2.1	−2.1	−2.1	−2.1	−2.1	−2.1	−2.1	−2.1	−2.1	−2.1	−2.1
3000	−1.7	−1.7	−1.7	−1.7	−1.6	−1.6	−1.6	−1.6	−1.6	−1.6	−1.6	−1.6	−1.6	−1.6	−1.6	−1.6
4000	−1.4	−1.4	−1.4	−1.4	−1.3	−1.3	−1.3	−1.3	−1.3	−1.3	−1.3	−1.3	−1.3	−1.3	−1.3	−1.3
5000	−1.2	−1.2	−1.2	−1.2	−1.1	−1.1	−1.1	−1.1	−1.1	−1.1	−1.1	−1.1	−1.1	−1.1	−1.1	−1.1
20000	−0.43	−0.43	−0.43	−0.43	−0.43	−0.42	−0.42	−0.42	−0.42	−0.42	−0.42	−0.42	−0.42	−0.42	−0.42	−0.42
200000	−0.08	−0.08	−0.08	−0.08	−0.08	−0.079	−0.079	−0.079	−0.079	−0.079	−0.079	−0.079	−0.079	−0.079	−0.079	−0.079
1000000	−0.024	−0.024	−0.024	−0.024	−0.024	−0.024	−0.024	−0.024	−0.024	−0.024	−0.024	−0.024	−0.024	−0.024	−0.024	−0.024

TABLE IX. Numerical results for the kite-diagram series (in mRy) generated using Monte Carlo integration method for many values of ζ and r_s covering the small r_s region, the large r_s region, and the physical region where materials are realized. (The standard deviations are reported in parentheses.)

r_s	$\zeta = 0$	$r_s \backslash \zeta$	0.2	0.4	0.6	0.8	0.9	1.0
0.01	47.60 (10)	0.2	40.75 (19)	40.85 (44)	41.66 (32)	42.83 (12)	43.3 (56)	44.44 (14)
0.09	44.16 (16)	0.4	36.23 (37)	37.37 (20)	37.77 (25)	39.24 (16)	39.5 (51)	42.30 (9)
0.1	43.53 (18)	0.6	33.79 (20)	34.31 (16)	35.02 (20)	36.85 (45)	37.6 (49)	39.89 (18)
0.2	40.85 (25)	0.8	31.2 (19)	31.75 (27)	32.68 (22)	34.46 (35)	36.0 (47)	37.76 (32)
0.3	38.45 (26)	1	27.77 (61)	29.42 (28)	30.09 (32)	32.46 (47)	33.6 (44)	36.43 (27)
0.4	36.00 (37)	1.2	26.41 (35)	27.79 (28)	27.59 (55)	30.34 (45)	32.2 (42)	34.83 (32)
0.5	34.26 (36)	1.4	23.90 (62)	25.51 (59)	27.08 (40)	29.68 (25)	31.0 (40)	34.05 (27)
0.6	33.90 (19)	1.6	23.10 (23)	24.02 (31)	25.37 (35)	27.10 (75)	29.7 (39)	32.65 (28)
0.7	31.89 (60)	1.8	21.62 (29)	21.38 (92)	24.49 (24)	26.79 (40)	28.9 (38)	31.71 (20)
0.8	30.2 (17)	2	20.55 (29)	21.63 (40)	23.23 (21)	25.73 (27)	27.5 (36)	30.46 (40)
0.9	28.79 (54)	2.2	19.29 (23)	19.67 (40)	21.95 (28)	24.23 (44)	26.9 (35)	29.48 (49)
1	27.62 (84)	2.4	17.04 (73)	18.66 (38)	21.12 (19)	24.26 (26)	25.5 (33)	28.80 (19)
2	20.31 (33)	2.6	17.08 (26)	17.44 (74)	19.69 (28)	21.97 (74)	24.6 (32)	27.82 (23)
3	14.85 (68)	2.8	16.16 (19)	17.28 (22)	18.96 (35)	22.02 (29)	24.5 (32)	26.90 (38)
4	10.56 (44)	3	14.58 (40)	15.97 (29)	17.01 (60)	21.18 (29)	23.3 (31)	25.93 (57)
5	8.04 (34)	3.2	14.02 (25)	14.17 (67)	16.63 (42)	20.41 (31)	22.18 (62)	24.71 (63)
6	5.07 (39)	3.4	13.27 (55)	14.41 (31)	16.44 (29)	19.70 (28)	21.6 (28)	24.81 (43)
7	2.23 (41)	3.6	12.13 (33)	13.17 (53)	15.82 (32)	18.91 (25)	21.0 (28)	23.81 (31)
8	0.78 (69)	3.8	12.14 (33)	12.61 (36)	14.97 (66)	18.34 (27)	20.3 (27)	23.47 (26)
9	−1.70 (72)	4	10.59 (49)	11.72 (51)	14.9 (22)	17.79 (22)	19.69 (23)	22.32 (44)
10	−2.11 (41)	4.2	9.81 (35)	11.35 (26)	13.53 (33)	17.14 (24)	18.8 (25)	22.21 (54)
20	−11.13 (90)	4.4	9.08 (67)	10.42 (29)	12.89 (28)	15.74 (38)	18.8 (25)	21.4 (13)
30	−14.85 (28)	4.6	9.01 (29)	9.50 (41)	11.95 (28)	15.47 (54)	18.26 (19)	20.87 (28)
40	−17.91 (46)	4.8	8.10 (56)	9.49 (27)	11.91 (18)	14.79 (58)	17.3 (23)	20.14 (71)
50	−19.45 (65)	5	7.49 (65)	8.59 (80)	11.58 (39)	14.21 (35)	16.1 (11)	20.04 (33)
60	−20.27 (43)	5.2	6.74 (51)	7.94 (39)	10.98 (30)	14.50 (29)	16.7 (22)	19.01 (35)
70	−21.67 (58)	5.4	6.17 (36)	7.68 (32)	10.47 (31)	12.99 (69)	16.1 (21)	19.13 (23)
80	−22.14 (28)	5.6	5.91 (43)	7.36 (22)	9.62 (26)	13.08 (37)	15.9 (21)	18.79 (24)
90	−22.62 (48)	5.8	4.85 (43)	6.17 (42)	8.54 (61)	12.78 (27)	14.8 (20)	17.18 (70)
100	−23.68 (80)	6	4.66 (59)	6.43 (27)	8.93 (30)	12.59 (21)	14.8 (20)	17.78 (24)
200	−25.09 (62)	10	−1.76 (57)	−1.00 (68)	2.01 (75)	3.9 (11)	8.20 (44)	8.8 (12)
300	−24.57 (25)	20	−13.0 (27)	−9.57 (67)	−6.71 (65)	−4.01 (48)	−2.5 (12)	1.35 (62)
500	−24.71 (49)	30	−15.18 (66)	−12.76 (31)	−11.0 (15)	−8.91 (50)	−7.59 (51)	−4.60 (49)
1000	−23.55 (36)	40	−17.05 (47)	−15.81 (47)	−14.76 (86)	−11.00 (42)	−9.56 (77)	−9.6 (22)
2000	−20.77 (48)	50	−19.25 (61)	−17.42 (38)	−16.01 (41)	−13.29 (65)	−12.02 (40)	−11.57 (82)
3000	−20.87 (73)	60	−20.47 (76)	−19.34 (44)	−18.42 (98)	−15.53 (52)	−13.72 (34)	−12.24 (47)
4000	−19.49 (22)	70	−22.0 (11)	−19.29 (31)	−17.92 (33)	−16.08 (45)	−15.10 (40)	−13.32 (33)
5000	−18.44 (18)	80	−21.38 (49)	−21.2 (32)	−19.7 (47)	−17.92 (53)	−17.15 (74)	−15.39 (39)
20000	−14.35 (22)	90	−22.46 (54)	−20.81 (31)	−20.28 (45)	−18.38 (55)	−17.31 (61)	−16.07 (33)
200000	−7.13 (15)	100	−23.15 (72)	−21.6 (15)	−21.01 (44)	−18.63 (43)	−18.60 (50)	−17.22 (58)
1000000	−3.89 (16)	200	−24.43 (49)	−23.43 (33)	−23.56 (79)	−22.46 (34)	−22.30 (47)	−21.97 (61)
		300	−24.24 (48)	−24.88 (50)	−24.06 (40)	−23.92 (57)	−24.04 (60)	−23.12 (48)
		400	−25.44 (76)	−24.10 (36)	−24.34 (29)	−23.52 (25)	−23.36 (30)	−24.33 (53)
		500	−24.28 (33)	−24.50 (43)	−24.89 (70)	−24.86 (70)	−23.49 (32)	−26.9 (22)
		1000	−23.56 (39)	−22.88 (28)	−23.11 (32)	−23.99 (48)	−23.94 (33)	−24.59 (62)
		2000	−21.16 (25)	−21.95 (70)	−22.18 (56)	−22.10 (21)	−22.88 (49)	−23.71 (36)
		3000	−20.16 (38)	−20.44 (22)	−20.46 (30)	−21.79 (50)	−21.69 (26)	−22.92 (36)
		4000	−19.45 (37)	−19.53 (24)	−20.06 (33)	−20.85 (29)	−20.76 (21)	−21.68 (23)
		5000	−19.76 (69)	−18.96 (27)	−19.86 (55)	−20.32 (77)	−20.15 (23)	−21.79 (45)
		20000	−13.98 (24)	−14.31 (21)	−14.58 (17)	−16.34 (56)	−15.93 (26)	−17.77 (47)
		200000	−7.00 (20)	−7.55 (19)	−7.46 (14)	−8.80 (30)	−9.06 (22)	−9.88 (30)
		1000000	−4.26 (39)	−3.78 (19)	−4.72 (25)	−4.41 (19)	−5.52 (32)	−5.56 (19)

[1] P. Hohenberg and W. Kohn, Inhomogeneous electron gas, Phys. Rev. **136**, B864 (1964).

[2] W. Kohn and L. J. Sham, Self-consistent equations including exchange and correlation effects, Phys. Rev. **140**, A1133 (1965).

[3] J. P. Perdew, K. Burke, and M. Ernzerhof, Generalized gradient approximation made simple, Phys. Rev. Lett. **77**, 3865 (1996).

[4] Y. Wang and J. P. Perdew, Correlation hole of the spin-polarized electron gas, with exact small-wave-vector and high-density scaling, Phys. Rev. B **44**, 13298 (1991).

[5] J. P. Perdew and Y. Wang, Accurate and simple analytic representation of the electron-gas correlation energy, Phys. Rev. B **45**, 13244 (1992).

[6] D. M. Ceperley and B. J. Alder, Ground state of the electron gas by a stochastic method, Phys. Rev. Lett. **45**, 566 (1980).

[7] G. Ortiz and P. Ballone, Correlation energy, structure factor, radial distribution function, and momentum distribution of the spin-polarized uniform electron gas, Phys. Rev. B **50**, 1391 (1994).

[8] G. Ortiz, M. Harris, and P. Ballone, Zero temperature phases of the electron gas, Phys. Rev. Lett. **82**, 5317 (1999).

[9] E. Wigner, On the interaction of electrons in metals, Phys. Rev. **46**, 1002 (1934).

[10] M. Gell-Mann and K. A. Brueckner, Correlation energy of an electron gas at high density, Phys. Rev. **106**, 364 (1957).

[11] P. Nozières and D. Pines, Electron interaction in solids. General formulation, Phys. Rev. **109**, 741 (1958).

[12] P. Nozeriés and D. Pines, *Theory of Quantum Liquids* (CRC Press, Boca Raton, FL, 1999).

[13] L. Onsager, L. Mittag, and M. J. Stephen, Integrals in the theory of electron correlations, Ann. Phys. (Berlin) **473**, 71 (1966).

[14] P. Giannozzi, O. Andreussi, T. Brumme, O. Bunau, M. B. Nardelli, M. Calandra, R. Car, C. Cavazzoni, D. Ceresoli, M. Cococcioni, N. Colonna, I. Carnimeo, A. D. Corso, S. de Gironcoli, P. Delugas, R. A. DiStasio, Jr., A. Ferretti, A. Floris, G. Fratesi, G. Fugallo *et al.*, Advanced capabilities for materials modelling with quantum espresso, J. Phys.: Condens. Matter **29**, 465901 (2017).

[15] P. Haas, F. Tran, and P. Blaha, Calculation of the lattice constant of solids with semilocal functionals, Phys. Rev. B **79**, 085104 (2009).

[16] F. Tran, R. Laskowski, P. Blaha, and K. Schwarz, Performance on molecules, surfaces, and solids of the Wu-Cohen GGA exchange-correlation energy functional, Phys. Rev. B **75**, 115131 (2007).

[17] J. S. Kang, M. Li, H. Wu, H. Nguyen, and Y. Hu, Basic physical properties of cubic Boron Arsenide, Appl. Phys. Lett. **115**, 122103 (2019).

[18] D. Pines, A collective description of electron interactions: IV. Electron interaction in metals, Phys. Rev. **92**, 626 (1953).

[19] D. Bohm and D. Pines, A collective description of electron interactions: III. Coulomb interactions in a degenerate electron gas, Phys. Rev. **92**, 609 (1953).

[20] A. L. Fetter and J. D. Walecka, *Quantum Theory of Many-Particle Systems* (McGraw-Hill, New York, 1971).

[21] G. Mahan, *Many-Particle Physics* (Kluwer Academic, New York, 2000).

[22] A. A. Abrikosov, L. P. Gor'kov, and I. E. Dzyaloshinski, *Methods of Quantum Field Theory in Statistical Physics* (Dover, New York, 1963).

[23] L. Hedin, New method for calculating the one-particle Green's function with application to the electron-gas problem, Phys. Rev. **139**, A796 (1965).

[24] J. J. Quinn and R. A. Ferrell, Electron self-energy approach to correlation in a degenerate electron gas, Phys. Rev. **112**, 812 (1958).

[25] P.-F. Loos and P. M. W. Gill, Correlation energy of the spin-polarized uniform electron gas at high density, Phys. Rev. B **84**, 033103 (2011).

[26] G. G. Hoffman, Correlation energy of a spin-polarized electron gas at high density, Phys. Rev. B **45**, 8730 (1992).

[27] S. Misawa, Ferromagnetism of an electron gas, Phys. Rev. **140**, A1645 (1965).

[28] D. Ceperley, Ground state of the fermion one-component plasma: A Monte Carlo study in two and three dimensions, Phys. Rev. B **18**, 3126 (1978).

[29] T. N. Mihm, B. Yang, and J. J. Shepherd, Power laws used to extrapolate the coupled cluster correlation energy to the thermodynamic limit, J. Chem. Theory Comput. **17**, 2752 (2021).

[30] D. L. Freeman, Coupled-cluster expansion applied to the electron gas: Inclusion of ring and exchange effects, Phys. Rev. B **15**, 5512 (1977).

[31] F. Coester and H. Kümmel, Short-range correlations in nuclear wave functions, Nucl. Phys. **17**, 477 (1960).

[32] H. Kümmel, Theory of many-body wave functions with correlations, Nucl. Phys. A **176**, 205 (1971).

[33] H. Kümmel and K. Lührmann, Equations for linked clusters and the energy variational principle, Nucl. Phys. A **191**, 525 (1972).

[34] G. Jansen, R.-F. Liu, and J. G. Ángyán, On the equivalence of ring-coupled cluster and adiabatic connection fluctuation-dissipation theorem random phase approximation correlation energy expressions, J. Chem. Phys. **133**, 154106 (2010).

[35] X. Ren, P. Rinke, G. E. Scuseria, and M. Scheffler, Renormalized second-order perturbation theory for the electron correlation energy: Concept, implementation, and benchmarks, Phys. Rev. B **88**, 035120 (2013).

[36] F. Hummel, A. Grüneis, G. Kresse, and P. Ziesche, Screened exchange corrections to the random phase approximation from many-body perturbation theory, J. Chem. Theory Comput. **15**, 3223 (2019).

[37] A. Dal Corso, Pseudopotentials periodic table: From H to Pu, Comput. Mater. Sci. **95**, 337 (2014).

[38] B. S. Shastry, Magnetic susceptibility of an electron gas in the random-phase approximation, Phys. Rev. B **17**, 385 (1978).

[39] K. A. Brueckner and K. Sawada, Magnetic susceptibility of an electron gas at high density, Phys. Rev. **112**, 328 (1958).

[40] D. R. Hamann and A. W. Overhauser, Electron-gas spin susceptibility, Phys. Rev. **143**, 183 (1966).

[41] Y. Zhang and S. Das Sarma, Exchange instabilities in electron systems: Bloch versus stoner ferromagnetism, Phys. Rev. B **72**, 115317 (2005).

[42] E. A. Brandes and G. Brook, *Smithells Metals Reference Book* (Elsevier, Amsterdam, 2013).

[43] H. Liang, L. Fang, S. Guan, F. Peng, Z. Zhang, H. Chen, W. Zhang, and C. Lu, Insights into the bond behavior and mechanical properties of Hafnium Carbide under high pressure and high temperature, Inorg. Chem. **60**, 515 (2021).

[44] L. Gerward, J. S. Olsen, L. Petit, G. Vaitheeswaran, V. Kanchana, and A. Svane, Bulk modulus of CeO_2 and PrO_2–an experimental and theoretical study, J. Alloys Compd. **400**, 56 (2005).